Chem Soc Rev

Combining Theories and Experiments to Understand the Sodium Nucleation Behavior Towards Safe Sodium Metal Batteries

Journal:	*Chemical Society Reviews*
Manuscript ID	CS-REV-01-2020-000033.R1
Article Type:	Tutorial Review
Date Submitted by the Author:	02-Apr-2020
Complete List of Authors:	Wang, Huan; Dartmouth College, Thayer School of Engineering Matios, Edward; Dartmouth College, Thayer School of Engineering Luo, Jianmin; Dartmouth College, Thayer School of Engineering Li, Weiyang; Dartmouth College, Thayer School of Engineering

Combining Theories and Experiments to Understand the Sodium Nucleation Behavior Towards Safe Sodium Metal Batteries

Huan Wang †, Edward Matios †, Jianmin Luo, Weiyang Li*

Thayer School of Engineering, Dartmouth College, Hanover, New Hampshire 03755, United States. Email: weiyang.li@dartmouth.edu

†These authors contributed equally to this review.

Abstract

Rechargeable sodium (Na) based batteries have gained tremendous research interests because of the high natural abundance and low cost of Na resources, as well as electrochemical similarities with lithium (Li) based batteries. However, despite the great potential as a candidate for the next-generation grid-scale energy storage, the implementation of Na metal anode has been primarily hindered by dendritic and "dead" Na formation that leads to low Coulombic efficiency, short lifespan and even safety concern. Na dendrite formation mainly originates from the uncontrolled Na deposition behavior in the absence of nucleation site regulations. Hence, the Na nucleation and initial stage of growth are critically important for the final morphology of Na metal. Here, this tutorial review aims to provide a comprehensive understanding on the importance of nucleation behavior towards dendrite-free Na metal anodes. Firstly, we start with an introduction about the advantages of Na metal batteries over the Li counterpart and the challenges facing by Na metal anodes. The differences between metallic Li and Na are summarized according to the advanced in-situ characterization techniques. Next, we elucidate the key factors that influence the Na nucleation and growth behaviors based on the existing theoretical models. Then, we review the state-of-the-art approaches that have been applied to effectively regulate Na nucleation for dendrite-free Na deposition. Lastly, we conclude the review with the perspectives for realizing safe Na metal batteries with high energy density.

Key learning points

(1) The advantages of Na-based batteries and current challenges of Na metal as anodes.

(2) Frameworks to describe the key factors that affect the Na nucleation behavior.

(3) Strategies of regulating Na nucleation site and growth pattern.

(4) Perspectives on the future developments of Na metal based batteries.

1. Introduction

The ever-increasing rate of fossil fuels consumption has already resulted in the urgent crises of energy insecurity and climate change. Meanwhile, the implementation of clean and renewable energy sources such as wind and solar have also expanded rapidly in the recent decade for a more sustainable future.[1] Nevertheless, renewable energy sources are intermittent and unpredictable due to the natural variation of cloud coverage and wind speed. Hence, cost-effective and reliable energy storage technologies are the key enabling factor for the seamless integration of fluctuating intermittent renewable energy to offset the consumption of fossil fuels. With the merits of outstanding energy conversion efficiency, compact size and low maintenance requirement, rechargeable lithium (Li)-ion batteries (LIBs) are one of the most cost-effective options for sustainable energy storage, as they have already dominated the market for portable electronics and electric vehicles (EVs). Particularly, EVs coupled with renewable energy sources play a crucial role for mitigating climate change and air pollution. As a result of burgeoning EVs industry, LIBs production is expected to grow significantly to meet the surging demand, which causes serious concerns regarding the future availability and cost of relevant raw materials. The abundance of Li is comparatively low in the Earth's crust (17 ppm), and the major Li reserves are located in the regions with unstable political and economic conditions.[2,3] Moreover, the Li extraction process is generally expensive, complicated, time-consuming and polluting. Therefore, it is necessary to find a more cost-effective energy storage technology alternative to LIBs.

As the second element in alkali metal group right below Li in the periodic table, Na not only possesses similar physical and chemical properties as Li, but also has major advantages over Li in terms of raw material availability and cost. Na-containing precursors are abundant worldwide, including sodium carbonate (Na_2CO_3), sodium sulfate (Na_2SO_4), and sodium chloride (NaCl), which are naturally deposited in minerals, brine and seawater. For instance, Wyoming has the largest deposit of Trona in the world, which can be mined as the primary source of Na_2CO_3, containing an equivalent of over 23 billion tons of Na_2CO_3. As a result, the Na_2CO_3 price is only \$0.5 kg^{-1}, far lower than Li raw materials ($LiCO_3$: \$6.5 kg^{-1}).[2] Furthermore, Na-based batteries have another advantage over the Li counterparts in terms of the cost and weight of the current collector. In LIBs, aluminum (Al) can only be used as the current collector for cathodes due to an alloy reaction between Li and Al at low potentials. Thus, the LIBs anode current collector has to be copper (Cu), which is much heavier and costly than Al. In contrast, Na

does not form alloy with Al, thus allowing Al to serve as current collectors for both anodes and cathodes to reduce cost and battery weight.

Based on the abovementioned merits, Na-based batteries have gained significant research interests. The development of Na-based batteries began with rechargeable molten-Na beta-alumina batteries, primarily including high-temperature Na-sulfur (S) batteries and Na-nickel chloride ($NiCl_2$) batteries with a high operating temperature between 270 to 350 ^oC. With molten salts as electrolyte and molten Na as anode, high-temperature Na-S batteries have been operated commercially for stationary energy storage.[1,3] However, multiple technological challenges such as harsh operating conditions, maintenance requirement and safety issues related to the molten Na metal leakage render these batteries impractical for large scale energy storage. Sharing the identical working principle and cell construction with LIBs, Na-ion batteries (NIBs) were developed side-by-side with LIBs in the mid-1980s, and research interest in NIBs has again revived since early 2010s.[1-5] Thus far, NIB cathode development has advanced significantly, with some of them exhibiting comparable performance to LIBs counterpart. However, NIB anode remains to be a grand challenge because it is not feasible to simply emulate the state-of-the-art LIB anode materials despite their similarities. For instance, graphite, the most widely used commercial LIB anode material, is not capable of hosting Na^+ due to thermodynamic instability.[6,7] Through extensive screening on promising Na anode materials, several types have been identified based on different mechanisms including alloy, conversion and insertion reaction.[1-5] Among them, hard carbon and other disordered carbonaceous can enable Na^+ intercalation because of the relatively large interlayer distance and disordered structure, therefore exhibiting great potential as anode candidates for NIBs. Furthermore, metal alloys, metal oxides/sulfides/phosphides and their analogues have been demonstrated as NIB anodes, albeit with the issues related to severe volume change and relatively high redox potential. Notably, research progress of both anodes and cathodes for NIBs have been comprehensively summarized in many excellent review articles.[3-5] Herein, we emphasize the discussion on the most promising anode material for high-performance Na-based batteries—metallic Na anode.

2. Current challenges of Na metal as anodes

Despite the intensive research efforts, the anode remains as the major constraint for NIBs to be on a par with the state-of-the-art LIBs. Similar to the role of Li metal anode in Li-based

batteries, Na metal is considered as the "holy grail" for Na-based batteries due to its high specific capacity (1166 mAh g^{-1}) and low electrochemical potential (-2.71 V vs. reversible hydrogen electrode). Specifically, Na metal can exclusively be paired with high-capacity Na-free cathodes, such as sulfur (S), oxygen (O_2), carbon dioxide (CO_2) and selenium (Se).[8-11] Thus, Na metal anode enables a wide variety of battery chemistries with high theoretical energy densities far exceeding those of the LIBs. Nevertheless, the practical implementation of Na metal anode is hindered by two main challenges associated with cyclability and safety, primarily originating from its high chemical reactivity and huge volume expansion that can ultimately lead to uncontrolled dendritic/mossy Na growth and propagation. The chemical potential of Na metal is above the lowest unoccupied molecular orbital of most liquid organic electrolytes, resulting in spontaneous electrochemical reduction of organic solvents by the highly reactive Na metal and the formation of passivation film on the Na metal surface referred as solid electrolyte interphase (SEI). The continuous formation and decomposition of SEI not only consumes the electrolyte and Na^+, but also induces the uncontrolled Na dendrite growth. In addition, the volume change of Na metal anode is relatively infinite due to its hostless nature, which can further aggravate Na dendrite growth and deteriorate the cell performance. Furthermore, Na dendrites can penetrate through a separator and cause short circuit, leading to overheating and possible fires. To overcome these challenges, various approaches have been developed toward the realization of high-performance, electrochemically robust and safe Na metal batteries.

Engineering Na anode surface with thin film coating, employing a matrix material to host Na metal and tuning electrolyte compositions are the typical strategies that have been summarized and highlighted in many excellent review papers.[8-10] Despite the extensive research achievements, most of the abovementioned approaches are result-orientated that mainly focus on the morphology evolution and overall performance of Na metal anodes. Meanwhile, strategies of mitigating or eliminating Na dendrites at the source are of equal or even higher importance. Therefore, it is necessary to have a comprehensive understanding on the nucleation behavior and early stage of Na growth in order to govern the final pattern of metallic Na deposition. In this regard, electrodeposition and thermal infusion are the two common methods to pre-store Na metal onto the current collector as a substrate for subsequent Na plating and stripping cycles. Particularly, it is important to employ Na metal anode in a close-to-stoichiometric amount with respect to the cathode in order to avoid excessive Na metal usage to minimize material waste and

prevent potential safety hazard during practical operation. However, Na^+ electrodeposition is susceptible to random Na nucleation and growth that leads to high nucleation overpotential and locally intensified current density and thereby dendrite growth. As to the thermal infusion method, poor wettability between the substrate and molten Na can cause discontinuous Na distribution and subsequent non-uniform Na stripping and plating with dendrite formation. In either case, a comprehensive understanding on Na nucleation behavior is essential to realize dendrite-free Na metal anodes.

Herein, this tutorial review focuses on the effect of nucleation behavior on the morphology and electrochemical performance of metallic Na anode from both theoretical and experimental perspectives. First, we assess the recent progress on advanced techniques for the in-situ observation of dendritic Na formation to elucidate the differences between Li and Na metal as well as the reason behind the relatively low Coulombic efficiency of metallic Na over electrochemical cycles compared to Li metal. Next, we present theoretical models to describe the Na deposition process by integrating the heterogenous nucleation and growth, fundamental thermodynamic principles and electrochemistry concepts. Then, we introduce the recently proposed strategies to identify the dominant factors for regulating nucleation sites towards dendrite-free Na metal anodes. Lastly, we provide perspectives for the future development of safe and high-performance Na metal batteries.

3. In-situ observation of Na deposits and the differences between Li and Na metal systems

Analogous to Li metal as an anode, Na metal can be repeatedly plated and stripped over cycles. The nucleation and growth behavior of Li metal has been well investigated through a variety of advanced in-situ characterization techniques along with several proposed models in order to develop novel solutions for suppressing Li dendrite growth, whereas the in-situ observation and mechanism study of Na metal deposition remains elusive. Even though Na and Li are the neighbors in alkali metal group with similar properties, the scientific challenges for the commercialization of Li metal anode vs. Na metal anode are inherently different and therefore thorough exploration and understanding on their respective electrochemical cycling behaviors are necessary.

Table 1. Property differences between element Li and Na.

Property	Parameter	Li	Na
Physical property	Atomic radius (Å)	1.52	1.86
	Atomic weight (g mol^{-1})	6.9	23
	Molar volume (cm^3 mol^{-1})	12.97	23.75
	Melting point (K)	454	371
	Ionic radius (Å)	0.76	1.02
	Abundance in Earth's crust (%)	0.0017	2.3
	Price (carbonate salt, $/ton)	17000	390
Chemical property	Electron configuration	[2,1]	[2,8,1]
	1st ionization energy (KJ $mol^{-1)}$	520.2	498.8
	Reactivity with Al	Yes	No
Electrochemical property	Voltage vs. RHE (V)	-3.0	-2.7
	Desolvation Energy with EC (KJ mol^{-1})	211.3	151.9
	Desolvation Energy with DEC (KJ mol^{-1})	207.7	147.5
	Desolvation Energy with PC (KJ mol^{-1})	218.0	157.3
Mechanical property	Bulk modulus (GPa)	11	6.3
	Brinell hardness (MPa)	5	0.69

Table 1 lists some major characteristic differences between Na and Li metals,[12,13] which can lead to entirely different electrochemical behaviors and thus battery performance. For instance, the relatively larger atomic radius of Na causes its outer shell electron to experience a weaker nucleus attraction compared to Li. In this case, Na can donate its electron more easily and thus have higher chemical reactivity. Therefore, Na can more acutely react with common organic electrolyte, making it more difficult to form a compact and uniform SEI on Na metal surface. Moreover, the as-formed SEI is mainly composed of Na salts, which are more susceptible to be dissolved possibly due to the weaker Lewis acid nature of Na ions. Consequently, the as-formed SEI on Na surface is very unstable and non-uniform compared to Li counterparts. Also, the relatively weaker mechanical modulus of Na can result in the greater vulnerability that is prone to continuous dissolution and dissociation of Na dendrites at the expense of organic electrolyte and active material, ultimately leading to "dead" Na formation.

Meanwhile, the weaker mechanical property of Na metal can be somewhat beneficial, as Na dendrites may be blunted and suppressed by a robust SEI layer and separator. Another major characteristic difference between Li and Na is that the extra electron shell results in a weaker charge density around Na ions with a lower Na^+ de-solvation energy, which makes the solvent molecule easily removable during Na^+ diffusion through SEI layer. This can facilitate a lower interfacial resistance and high ionic conductivity that is beneficial for Na deposition behaviors at high current densities compared to Li metal system. Because of the property differences between Li and Na metal, one cannot simply emulate the strategies for stabilizing Li metal toward Na metal, hence the stabilization strategies for Na metal must be specially designed (Table S1).

Generally, the information gained from ex-situ methodologies are limited to before and after cycling, and thus no valuable insights can be obtained during the operation of a Na metal battery. Consequently, it is very difficult to gather critical information on dynamic or transient states formed during battery working state, which may lead to erroneous conclusions. By comparison, in-situ characterization techniques can monitor the real-time reaction that occurs under operando conditions, allowing a comprehensive understanding on the Na nucleation and growth dynamics. In this section, we summarize the recent works on the observation of Na deposition during electrochemical process through operando techniques.

Optical microscopy (OM) is a convenient and useful tool to trace the evolving Na morphology at microscopic scale during charging and discharging process. Archer and coworkers performed the in-situ optical visualization measurements under galvanostatic plating/stripping conditions.[14] The deliberate cell design allows the image collection of changing Na morphology at different time points throughout plating and stripping process. The chronological imaging revealed that the mossy Na deposits with extremely soft and fragile nature are susceptible to physically breakage, detach from bulk Na electrode and then lose electronic connection with the underlying/bulk Na electrode followed by orphaned Na formation and irreversible Na metal loss (Figure 1a). Hence, the in-situ visualization technique provides valuable information about Na metal morphology evolution over cycling, providing evidences to counter the erroneous conclusion that Na electrode can be highly reversible based on the morphology before and after cycles. Specifically, Na metal cell failure is largely caused by the physical loss of active anode material and continuous electrolyte consumption needed to regenerate the SEI. The battery failure mechanism observed from Na metal cycling is different

from Li metal case, in which the dendritic Li can penetrate through a separator and therefore cause the cell short circuit. These differences mainly originate from the fact that metallic Na bulk and dendrites are both notably softer than the Li counterparts.

To further compare the differences between metallic Na and Li systems, in operando optical observation were carried out under quasi-zero electrochemical fields in symmetric Na and Li cells, respectively.[13] Results show that the Na metal soaked in carbonate-based electrolytes exhibits rough pits and heaves compared to a pristine Na metal, indicating the continuous side reaction between Na metal and electrolyte due to the higher chemical reactivity and less stable SEI formation. In sharp contrast, Li dendrites underwent relatively little changes under identical condition. Thus, the fact that Na dendrites can be gradually dissolved and disappeared in electrolyte revealed an obvious difference in the mechanical rigidity between Na and Li metal dendrites (Figure 1b). These observations indicate that Na dendrites and SEI are mechanically unstable due to its weaker chemical bonding and higher chemical activity. Accordingly, the symmetric Na cells exhibit more pronounced fluctuating voltage hysteresis and more serious polarization in comparison to the Li ones, verifying that the nature of Na dendrites and SEI are fundamentally different from the Li counterparts.

In-situ atomic force microscopy (AFM) is a powerful tool to provide nanoscale information on the electrode surfaces, and it has been employed to investigate Na metal deposition behavior in combination with an equipped optical camera.[15] Three stages of Na deposition: nucleation, growth and dendrite formation were proposed based on the Na deposition morphology change during various plating periods (Figure 1c). Similar to the observation made from the in-situ OM study, inactive Na formation occurred as metallic Na breaks away from the bulk, resulting in low Coulombic efficiency. Overall, in-situ AFM further confirm that the challenge associated with dendritic Na metal is more severe than Li metal case.

In-situ nuclear magnetic resonance (NMR) spectroscopy presents a valuable and non-invasive analysis technique to provide real-time and quantitative information on the dynamic processes, metastable phases as well as structural changes upon cycling. In-situ NMR analysis of ^{23}Na on symmetrical Na cells under galvanostatic conditions can provide information about Na metal growth mechanism and monitor microstructure formation (Figure 1d).[16] Based on the ^{23}Na NMR signal intensity, the relationship between dendritic microstructures and current densities can be elucidated, and thus two types of regimes for the electrochemical cycling of Na metal

were observed: (*i*) during lower current density cycling (i.e. ≤ 0.5 mA cm^{-2}), a time-dependent progressive nucleation mode is predominant with a lower overpotential, and the stripping of as-plated dendritic microstructures is highly reversible; (*ii*) at a higher current density cycling (i.e. ≥ 1 mA cm^{-2}), Na deposition shows a tendency toward time-independent and instantaneous nucleation, and the stripping efficiency of as-plated dendritic microstructures is dramatically decreased. With this information, it becomes feasible to mitigate dendritic microstructures and thus prevent cell short circuit through adjusting the operating parameters.

Despite the advances in in-situ characterization techniques for electrochemical Na plating/stripping, the essential information on Na initial nucleation mode and growth behavior still remain unavailable. Overall, according to the in-situ characterization studies, the following conclusions can be drawn. Firstly, compared to Li metal, the challenges related to Na dendrite growth and "dead" Na formation are more severe due to its more reactive nature and weaker mechanical property. Secondly, metallic Na deposition dynamics as well as the final morphology are quite different from the observations for Li metal, and hence further investigation is highly desirable. Therefore, it is imperative to gain further fundamental insights on the Na nucleation behavior to better understand the subsequent growth pattern and electrochemical performance.

4. Framework to describe Na nucleation and growth during electrodeposition process

Based on the principles of transitional metal (*e.g.* Co, Ni) deposition and the existing framework for Li metal deposition behavior,[17-19] this review presents a general guideline to describe Na heterogenous nucleation and subsequent growth behavior by integrating classic film growth theory and electrochemistry concepts. Furthermore, key factors including thermodynamic and kinetic aspects are discussed for their respective roles in influencing Na nucleation and growth, thereby providing insights for designing effective strategies to restrict Na dendrites.

Na ions deposition takes place as they migrate across a SEI layer and gain electrons from a current collector, and this process is subjected to a heterogenous nucleation behavior. Thus, Na nuclei can be depicted as a spherical cap-shaped cluster with radius (R) and a contact angle (Θ) on an underlying substrate (Figure 2a). From thermodynamic point of view, the formation of a new nucleus can result in a change in Gibbs free energy (ΔG) that is balanced by two competitive factors between volume free energy (negative) and interfacial energy (positive) for a new solid phase formation. For Na electrodeposition on a current collector, the electric field can

also contribute to Na nucleation and growth on a heterogeneous substrate. Thus, the ΔG value accompanied with the formation of Na nuclei can be expressed as follows:

$$\Delta G = -\frac{4}{3}\pi R^3(\Delta G_v + \frac{F\eta}{V_m}) + 4\pi R^2\gamma_{NE} \qquad (1)$$

Where ΔG_v, F, V_m, γ_{NE}, η and R represent Gibbs free energy per volume, Faradaic constant, molar volume of Na, surface energy of Na nuclei and electrolyte interface, overpotential and nuclei radius, respectively. A nucleus evolves from a so-called embryo that needs to reach a minimize radius, known as the critical radius, in order to be thermodynamically stable. From a mathematic perspective, as $\frac{\partial_{\Delta G}}{\partial_R}$ becomes more negative, the embryos are more stable toward subsequent growth accompanied with a decrease in Gibbs free energy (thermodynamically favorable). On the other hand, the value of ΔG_v reaches zero as nucleation takes places. Thus, the critical radius (R_{crit}) of Na nuclei can be expressed by the following equation:

$$R_{crit} = \frac{2\gamma_{NE}V_m}{F|\eta_n|} \qquad (2)$$

where η_n represents the nucleation overpotential on an electrically charged current collector. Evidently, the critical size is closely related to the surface energy and nucleation overpotential. In the following context, we focus on these two factors to discuss their respective roles in affecting the Na nucleation behavior. Note that the evolution and subsequent growth of Na nuclei can only take place in regimes where the embryo size is greater than the critical radius.

In classic crystal growth theory, supersaturation is considered as the relatively uncontrollable driving force that affects the rate of nucleation. During electrodeposition, the magnitude of supersaturation ($\Delta\mu$) can be largely determined by the overpotential on a working electrode with a relationship as follows: [20]

$$\Delta\mu = zF\eta - RT\ln\frac{\left[Na^+\right]_{El}}{\left[Na^+\right]} \qquad (3)$$

where $[Na^+]_{El}$, $[Na^+]$, z, F, η, R and T denote the local Na ions concentration near the current collector, local Na ions concentration in the bulk electrolyte, number of electrons exchanged, Faradaic constant, overpotential, ideal gas constant and temperature, respectively. The $[Na^+]_{El}$

value may vary over time or upon location, allowing for variations of the supersaturation. The equation also indicates that the overpotential varies over time even under constant current density, which is depicted in Figure 2b. A very steep drop in the positive voltage range possibly involved SEI formation can be observed at the beginning of discharge. This is a typical overpotential behavior unless there is alloying or intercalation reaction, which can be identified by a much more gradual voltage drop over a correspondingly longer time under galvanostatic deposition. Generally, the voltage continues to decrease initially and followed by a gradual increase with Na plating reaction before reaching a stable negative voltage plateau. As a result, an overpotential spike induced by the local electric field for the heterogenous nucleation is presented at the early stage of Na plating process, reflecting the electrochemical supersaturation needed to overcome the nucleation barrier in order to initiate a stable Na embryo formation. This means that a voltage dip in the voltage profile of the 1st cycle is related to the nucleation potential (η_n) that can be estimated by the differences between the bottom of the voltage dip and the voltage plateau afterward. In other words, overpotential is a vital kinetic factor that dictates the nucleation process, nucleus size, nucleation rate and time, therefore the Na deposition pattern. The plateau potential (η_p) stands for the energy barrier for subsequent Na growth.

The difference between nucleation potential and plateau potential can be used to evaluate the related nucleation mechanism. Based on Scharifker and Hills (SH) model proposed by Palomar-Pardavé *et al.*, the nucleation mode mainly involves instantaneous nucleation and progressive nucleation, which can be determined by potentiostatic current-time transient measurements combined with theoretical values.[21] For the instantaneous nucleation, nuclei are formed almost simultaneously and the subsequent process is predominated by nuclei growth. In the case of progressive nucleation, growing numbers of nuclei are constantly being formed not only on the substrate surface but also on previously formed nuclei throughout the entire deposition process. For most reported deposition studies that are conducted under galvanostatic conditions, a high driving force (high energy barrier) is needed to initiate the heterogenous nucleation. As a result, there is an obvious difference between the nucleation overpotential and growth potential, indicating that the nucleation mode follows an instantaneous process. Moreover, equation (2) indicates that the critical radius has an inverse relationship with overpotential, implying the drop in overpotential can increase the critical radius of the nuclei. In this case, any embryos smaller than the critical radius are not stable and therefore cannot survive

in the following electrochemical process. Thus, decreasing overpotential can result in a lower nucleation density, rendering the nucleation process in a more controlled manner that is favorable for uniform Na deposition.

Meanwhile, with the decrease in nucleation overpotential, the difference in energy barrier between nucleation and growth becomes smaller. As a result, the nucleation process tends to follow a progressive nucleation mode. In this regard, a study was conducted on Na nucleation process assisted by embedded carbon network to promote a progressive nucleation mode that enabled a lower Na nucleation overpotential and uniform deposition.[22] Overall, the nucleation mode can be used to determine the nucleation rate and active sites density from the kinetic perspective. Nevertheless, more in-depth studies are required for a comprehensive understanding of the initial Na nucleation behavior.

4.1 Kinetic factors

From a kinetic perspective, electrodeposition process can be divided into three stages: charge transfer, diffusion, nucleation and electro-crystallization (activation). Thus, the overall barrier for nucleation involves the charge transfer overpotential (η_t), diffusion overpotential (η_d), nucleation overpotential (η_n) and crystallization overpotential (η_a):

$$\eta = \eta_t + \eta_d + \eta_a + \eta_n \quad (4)$$

For galvanostatic Na deposition, the charge transfer overpotential can be neglected. Barton *et al.* proposed the following theoretical framework to describe the nucleation barrier by integrating the above-mentioned contributors.[20]

$$\eta = \frac{i}{i_0}\frac{RT}{F} + \frac{irRT}{DcF^2} + \frac{2\gamma_{NE}V_m}{Fr} \quad (5)$$

where η, i, i_o, D, c, R, r, F, T, V_m and γ_{NE} are the total overpotential associated with the Na nucleation, current density, exchange current density, Na^+ diffusion coefficient, Na^+ diffusion concentration, universal gas constant, radius of nucleation tip, Faradaic constant, temperature, molar volume of Na and nuclei/electrolyte interfacial energy, respectively.

Although it is difficult to deconvolute the magnitude of each of the abovementioned contribution towards Na nucleation, the current density (i) clearly acts as a crucial and dynamic parameter for initiating Na nucleation. Besides adjusting the applied current density, substrate morphology and structure can affect the magnitude and distribution of current density. Hence,

nanostructured or three-dimensional (3D) current collectors can be employed to dissipate local current density and lower the Na nucleation overpotential by increasing the surface area, which can concurrently alleviate the volume change upon cycling. Additionally, the surface conditions of underlying substrate can dictate the nucleation and initial plating behavior. The surface supersaturation of Na ions can be more readily achieved on these locations containing impurities and defects, generating the localized "hot spots", where Na preferentially nucleates and grows.

In addition, the self-diffusion of atoms has long been considered as a critical factor in deposition morphology as well as electrodeposition behavior. Previous studies show that the density of metal islands during electrodeposition is inversely proportional to the surface diffusion coefficient, which can be evaluated by the surface self-diffusion barrier. Specifically, the difference between surface diffusion barrier and interlayer diffusion barrier is known as Ehrlich-Schwoebel barrier (E_{ES}), and therefore a small E_{ES} indicates a large surface diffusion barrier. The relatively small E_{ES} for Na metal indicates that the large interlayer diffusion barrier is the dominant factor for Na deposition morphology. It was found that fractal growth of Na metal is favored as Na metal has a relatively high interlayer diffusion barrier. As a body-centered cubic metal, Na favors the lower-coordinated configurations.[23] These features synergistically lead to the formation of rough surface with dendritic Na structures upon electrochemical deposition.

Due to the instantaneous chemical reaction between Na metal and electrolyte, a SEI layer generally forms prior to Na nucleation. Under an electric field, the de-solvated Na ions migrate through the as-formed SEI layer and gain electrons, followed by the nucleation and deposition between SEI layer and the underlying current collector. Hence, the SEI thickness and composition can affect the transport pathway of Na ions, ultimately dictating Na nucleation behavior. Because of the complicated structure and lack of reliable in-situ experimental techniques, the study on SEI formation mechanism and process in Na metal system is still in its infancy. Yet, it is widely accepted that a SEI layer is a mixture of multiphase products, making it very difficult to generate uniform and compact passivation layers. Thus, the Na-ion transport across a SEI onto an underlying substrate can be significantly affected, rendering non-uniform distribution of Na nucleation site and possible dendrite formation. Since the as-formed SEI is highly dependent on the compositions of liquid electrolyte,[8-10] both the solvent and salt of liquid electrolytes play an important role in the homogeneity and ionic conductivity of SEI, thus affecting the Na^+ diffusion ability and flux distribution. Additionally, the salt complexes and

concentrations can impact the de-solvation energy of Na-complex ions before diffusion across SEI.[19] Hence, the property of liquid electrolyte can have major influence on the kinetics of Na nucleation. To date, many result-orientated strategies on forming uniform SEI layer have been proposed to simultaneously block the side reaction between Na metal anode and electrolyte via tuning electrolyte compositions.[8-10] Nevertheless, the role of liquid electrolyte on the initial nucleation behavior is often neglected, and this area requires further studies.

Aside from tuning electrolyte compositions, various kinds of artificial SEI films have been developed as a physical inhibitor to suppress Na dendrite growth (Table S2). However, only a handful of studies have attempted to understand the role of SEI compositions in affecting surface diffusion kinetics of Na ions as well as the initial nucleation behavior on a current collector. In this regard, Archer and coworker investigated the relationship between SEI chemistry and surface diffusion barrier for Na ions by the means of joint density-functional theory (JDFT) calculations and experiments.[24] Their results show that a SEI composed of sodium bromide (NaBr) presents an exceptionally low energy barrier for interfacial Na^+ transport, resulting in superiorly stable cycling behaviors with constantly low overpotential and high Coulombic efficiency over long-term cycles with dendrite-free Na metal surface after cycling (Figure 3). This work reveals that SEI chemistry plays an importantly role in Na-ion diffusion, while detailed Na nucleation behavior still requires further studies. Particularly, SEI layer breakage due to volume expansion can exacerbate localized current density that promotes dendrite formation, and therefore Na-ion flux behavior and Na nucleation pattern should be considered for in-depth research. Overall, robust and ultrathin SEI films with high Na^+ conductivity and homogeneity are one of the essential requirements for uniform Na nucleation.

4.2 Thermodynamic factors

The formation of a new phase can lead to increasing surface energy, which is defined as the work required to increase the surface area of a new phase by unit area. As a thermodynamic factor, the surface energy alone cannot dictate the critical radius, but can affect the overpotential barrier that varies significantly depending on the chemistry of an underlying substrate. A high surface energy between Na nuclei and electrolyte is favorable for the realization of a low energy barrier for Na nucleation. A wettability test can be used to determine the substrate surface energy,

while the contact angle can be used to quantitively evaluate the surface energy. According to the Young's equation, the contact angle can be expressed as the following equation:

$$\cos\theta = \frac{\gamma_{SE} - \gamma_{NS}}{\gamma_{NE}} \qquad (6)$$

γ_{SE}, γ_{NS} and γ_{NE} stand for the substrate surface energy, nuclei surface energy and nuclei/electrolyte interfacial energy, respectively. Generally, a low surface energy cannot form a strong bond with molten Na metal, leading to a poor Na wetting behavior and therefore a large contact angle. On the contrary, excellent molten Na spreading can occur with a small contact angle for a surface with a high surface energy. Similar to a water droplet on a substrate, sodiophobicity behavior can be revealed by a large contact angle between molten Na and underlying substrate, while a small contact angle suggests sodiophilicity behavior. For thermal infusion method, the macroscopic observation on the spreading of molten Na on a substrate is a general guideline for evaluating the wettability and surface energy. If a reaction occurs during this process, the change in Gibbs free energy of the reaction (ΔG_r) can also contribute to the molten Na spreading,[25] resulting in a smaller contact angle. This phenomenon can be expressed by the following equation：

$$\cos\theta_r = \cos\theta - \frac{\Delta\gamma_{SE} + \Delta G_r}{\gamma_{NE}} \qquad (7)$$

where θ_r stands for the contact angle after reaction, and $\Delta\gamma_{SE}$ represents the change in interface energy between a substrate and electrolyte due to a new phase formation. Accordingly, a more negative ΔG_r value and a decrease in γ_{SE} can lead to a small contact angle, thus a better wettability. While for the adsorption reaction, $-\Delta G_r$ corresponds to the binding energy between Na and the substrate. Hence, a high binding energy can lead to good wettability, as illustrated in Figure 4. Therefore, the most common method for tuning surface energy is through surface treatment, including thin film coating, implantation of nano/micro-scale species that can react with Na metal or possess high binding energy with Na metal.

The reaction spontaneity in thermodynamics is governed by the change in Gibbs free energy (ΔG_r), which is sensitive to temperature, as shown in the following equation.

$$\Delta G_r = \Delta H - T\Delta S \qquad (8)$$

ΔH and ΔS represent the enthalpy and entropy change of the reaction, respectively. Metallic Na possesses a relatively smaller ΔH compared to Li metal because of their ionic energy differences. Meanwhile, increasing temperature can reduce the viscosity of molten Na and therefore lead to a higher ΔS. Generally, higher reaction temperature (infusion temperature) can result in a more negative ΔG to promote a smaller contact angle and a better wettability. The thermal infusion of Na usually occurs at a temperature slightly above Na melting point. In additional to their different chemical properties, the melting point of metallic Na (~370.9 K) is much lower than that of Li metal (~453.7 K), and hence their respective molten states are likely to exhibit different wettability behaviors on the same substrate. It was discovered that the wettability of molten Na on a bare titanium (Ti) foil is much better than molten Li.[26] This observation is due to a smaller ΔH as well as a lower viscosity of molten Na than that of molten Li at the same temperature, and therefore molten Na has a higher ΔS value and a more negative ΔG_r. In contrast, gold (Au) film coated substrate exhibits a better wettability with Li than that of Na, theoretically due to a more negative ΔG of the Au-Li alloying reaction, leading to a smaller contact angle and higher driving forces for the spreading of molten Li. Based on the above discussion, we compare the differences of nucleation and growth behavior between Li and Na metal in Table S3.

Nevertheless, the reaction between Na metal and the coated film can cause a severe volume expansion, leading to electrode degradation. To address this issue, the introduction of sodiophilic nanoscale particles on a current collector can be effective in restricting volume expansion by providing nanoseeds for guided Na nucleation and growth. Meanwhile, sodiophilic phases can be formed in-situ during the alloying reaction to further decrease the contact angle and therefore enabling an excellent wettability and a lower Na nucleation barrier. Additionally, engineering heteroatom dopants or functional groups on a current collector can also lead to a high binding energy with Na and therefore a lower Na nucleation barrier through increased adsorption reactions. From theoretical calculations, the chemical or adsorption reaction can be quantitatively described by the binding energy between Na atoms/clusters and underlying substrate surface to lower the energy barrier for Na nucleation.

5. Nucleation-controlled strategies to regulate Na deposition

Based on the above framework, current density and surface chemistry are the two key factors for regulating the Na nucleation behavior kinetically and thermodynamically, respectively. In this regard, in this section we focus on the recent progress on tuning nucleation behaviors towards dendrite-free Na metal anodes. Notably, many of the strategies combine both current density and surface chemistry factors for Na nucleation regulation.

5.1 Planar Substrate

Pint's group conducted the pioneering work on the nucleation-controlled Na plating through coating nanocarbon on Al current collector to facilitate Na seeding process.[27] Compared to bare Al, the nucleation energy barrier was greatly decreased with the coated nanocarbon layer, leading to improved Na nucleation and deposition behavior and morphology (Figure 5a). As a result, an average Coulombic efficiency of 99.8% was achieved with a lower voltage hysteresis and smoother Na morphology over long-term cycles (Figure 5b, c). Moreover, excellent performance with energy densities of ~400 Wh/kg is demonstrated in a full cell with a pre-sodiated pyrite cathode. Afterwards, Li's group carried out a fundamental study to reveal the Na nucleation and growth behaviors through the use of well-defined planar two-dimensional doped and pristine graphene film as substrates (Figure 5d).[28] In this work, theoretical calculations were carried out to reveal that boron (B) dopants in B-doped graphene and their surrounding areas have high binding energy with Na atoms to serve as preferential nucleation sites for Na plating (Figure 5e). As a result, B-doped graphene enables a lower Na nucleation barrier and higher binding energy (Figure 5f). Accordingly, a stable cycling behavior with a low voltage hysteresis and uniform Na plating with dendrite-free Na morphology over long-term cycles can be achieved on B-doped graphene film in both ether-based electrolyte and quasi-solid polymer electrolyte (Figure 5g, h). Based on the stable B-doped graphene/Na anode, Na-S and Na-Co_3O_4 full cells showcase improved electrochemical performance.

Since common Al and Cu substrates have negligible solubility in Na, a relatively high nucleation overpotential can be observed especially on planar substrates, resulting in non-uniform Na nuclei distribution. Mao et al introduced a thin Au layer on Cu substrate (Cu@Au) to improve the sodiophilic property through the Au-Na alloy layer formation (Figure 6a).[29] In this manner, the energy barrier for Na nucleation can be effectively decreased to facilitate a uniform Na deposition with an average Coulombic efficiency of 99.8% in ether electrolytes over 300

cycles at a current density of 2 mA cm^{-2} (Figure 6b, c). This concept can also be applicable for tin (Sn) and antimony (Sb) film coating to form alloys with Na that exhibit greatly reduced nucleation overpotential for Na deposition (Figure 6d, e).[30] However, without the presence of a robust and porous host, the as-formed sodiophilic layer is susceptible to mechanical rupture during the repetitive alloying and dealloying process. To address this issue, Mao and co-workers subsequently demonstrated a strategy by controlling both the cutoff potential and the utilization of anchored sodiophilic particles to prolong the lifespan of Na metal to 2000 cycles with an average Coulombic efficiency of 99.9% (Figure 6f, g).

5.2 3D Porous Hosts

Similar to the development of Li metal anodes, utilizing 3D hosts with high surface area is considered as a straightforward approach to lower the nucleation barrier and therefore facilitate uniformly distributed Na-ion flux. The magnitude and distribution of current density can both impact Na nucleation behavior. Thus, 3D porous host can reduce local current density and ensure uniform Na nucleation and deposition. Meanwhile, they can also alleviate the major challenge of volume change over cycles. Compared to Li metal, Na metal is subjected to lower metallic binding energy and poor mechanical property that results in the challenge of maintaining good electrode structural integrity over cycles. Also, Na is mostly available in the form of Na ingot, requiring additional manufacturing process that can compromise the reproducibility and performance of Na metal anode. For these reasons, several types of hosts including porous Al (Figure 7a), Ag nanopaper (Figure 7b), carbonized wood (Figure 7c), carbon felt (Figure 7d), nanocrevasse-rich carbon fibers (Figure 7e), and carbon fiber scaffold (Figure 7f) have been developed by various groups to enable uniform Na deposition and stable cycling for dendrite-free Na metal anodes.[31-36] However, a fundamental understanding on their intrinsic properties including defects, impurity, passivation layer and pore size is still missing. There is a general consensus that the wettability between Na metal and a host material is the key factor for Na nucleation overpotential. In this case, a series of surface engineering approaches including chemically engineering interphase composition, introducing functional groups or dopants, regulating defects, employing alloy-based 3D hosts and implanting seed-guided sites have been proposed to optimize the sodiophilic nature of 3D hosts to nip the Na dendrite in the bud.

5.2.1 Chemically Engineering Interphase

3D porous Cu is a commonly used substrate for studying Li deposition behavior, however the effect of surface impurity or chemical residual on alkali metal deposition is still unclear. To address this knowledge gap, Li's group conducted a systematic study to elucidate the relationship between matrix interfacial property and Na anode electrochemical stability through oxidation or sulfurization treatment of commercial 3D Cu matrix (Figure 8a).[37] Experimental results suggested a surface-treated porous Cu skeleton can significantly increase its affinity toward molten Na due to a negative ΔG value in the chemical reaction between Na and the treated Cu. According to equation (7), the contact angle becomes smaller with an improved Na wettability that can facilitate uniform Na infusion and distribution. In contrast, the untreated Cu matrix shows poor wettability with molten Na. When compared with sulfur (S)-treated Cu matrix, the O-treated one shows a notably better wettability of molten Na due to a more negative ΔG from the reaction between molten Na and oxygen (O)-treated Cu than that of molten Na and S-treated Cu (Figure 8b, c). As a result, the O-treated Cu matrix exhibits the most stable voltage profile with the lowest overpotential for Na deposition over the repeated stripping and plating cycles (Figure 8d). The kinetic barrier for nucleation and subsequent growth can be largely reduced, as validated by *Deng et al.* in their subsequent work that used Cu_2O modified Cu foam with a high specific surface area to effectively reduce local current density and heterogeneity.[38] With $Na_3V_2(PO_4)_3$ as cathode, a full cell using O-treated Cu matrix/Na composite as anode shows superior cycling performance and rate capability compared with bare Na metal as anode.[37]

5.2.2 Introduction of Functional Groups and Heteroatom Dopants

Compared to metallic current collectors, 3D carbonaceous materials have the advantages of light weight, high electrical conductivity, good mechanical strength, and large specific surface area. Hence, 3D carbonaceous materials have been widely used as interface engineering layers or Na hosts. However, as most pristine carbon frameworks have a poor affinity with Na, Na deposition occurs mostly on the surface, rather than into the interior of the carbon host. As a result, Na preferentially grows onto the exoskeletons of carbon host and thus forms Na agglomerations, resulting in inhomogeneous Na deposition and high overpotential especially at high current densities. To improve Na wettability within carbon materials, functional groups and heteroatom dopants can be implemented to alleviate the wettability issue.

Inspired by the adequate wettability between reduced graphite oxides (r-GO) and Li metal, r-GO has also been employed as a Na metal host. Luo *et al.* fabricated a facile and moldable composite Na metal anode by infusing molten Na into the interlayers between r-GO sheets (Figure 9a).[39] Remarkably, the molten Na can quickly be absorbed into the r-GO interlayers upon contact, forming Na anodes and r-GO (Na@r-GO) composite with greatly enhanced mechanical strength for stable cycling in both ether and carbonate electrolyte with suppressed dendrite formation and negligible volume change (Figure 9b, c). It is believed that the r-GO surface groups such as carbonyl and alkoxy groups have stronger binding interactions with Na, which can reduce contact angle and improve wettability with molten Na as described in equation (7), promoting a low heterogenous Na nucleation overpotential and uniform deposition. Notably, this strategy is also feasible in potassium metal anodes, which indicates the importance of interface chemistry in regulating uniform alkali metal deposition.[40] *P*eng *et al.* hence reported the use of an oxygen-functionalized 3D carbon nanotube (O_f-CN) networks to create a sodiophilic interphase for improving binding affinity with Na (Figure 9d).[41] As a result, the as-obtained O_f-CNT network can provide abundant and homogeneous active sites to guide initial Na nucleation and navigate the subsequent growth (Figure 9e). Therefore, the networked O_f-CNT enables a homogenous Na nucleation at a lower overpotential to realize high capacity and long cycle-life Na metal batteries with dendrite-free morphology (Figure 9f-h). Furthermore, Na-air battery with Na@O_f-CNT as anode shows a five-fold improvement on cycling performance over 100 cycles and enhanced rate performance compared with bare Na metal anode.

Doping carbon matrix with heteroatoms is an established strategy to modify the electron density distribution and alter the binding energy toward Na atoms. The introduction of dopants can enhance the interaction between carbon matrix with Na metal to increase the binding energy with Na and lowers the contact angle, therefore improving Na wettability and guiding Na nucleation behavior. In this regard, a series of heteroatom dopants including B, nitrogen (N) and S have been successfully embedded into the carbon network for a low energy barrier for Na nucleation and stable Na deposition. Wang and co-workers employed thermal pyrolysis method for the synthesis of N and S co-doped CNT (NSCNT) papers as an interlayer to optimize Na nucleation behavior for uniform Na growth without dendrite formation (Figure 10a).[42] DFT calculation shows that the introduction of both N and S containing functional group can significantly increase the binding energy with Na atoms compared to Cu, Al and CNT (Figure

10b). As a result, the NSCNT possesses highly sodiophilic property. With the assistance of porous CNT, the as-prepared NSCNT paper can facilitate initial Na nucleation with low overpotential and direct uniform Na distribution, indicating the successful control of Na plating during nucleation stage (Figure 10c). Consequently, the Na/NSCNT composite anode exhibits a high reversibility and excellent cycling stability with a low voltage hysteresis and dendrite-free morphology during the repeated Na plating/stripping cycles (Figure 10d-f). As a proof of concept, the electrochemical performance of Na-O_2 cell with Na/NSCNT as anode is significantly more superior than that with bare Na anode.

In a separate effort, Sun *et al.* designed a carbon paper (CP) with N-doped CNTs (CP-NCNTs) as a 3D skeleton for stable use of Na metal anodes by taking advantages of N dopants as sodiophilic sites and the highly conductive networks to homogenize current density (Figure 10g).[43] Consequently, the Na@CP-NCNTs composite anode exhibits a uniform deposition morphology and stable cycling behavior at a high current density of 5 mA cm^{-2} and a capacity of 3 mAh cm^{-2} in carbonate electrolytes with low overpotential (Figure 10h, i).

5.2.3 Engineering Defects

Topological and edge defects are ubiquitous in pristine carbon materials, which are highly dependent on the material processing temperature. In general, a higher heating temperature can lead to larger domains with sp^2 bonded graphitic structure. In contrast, a lower heating temperature can result in an amorphous carbon structure that is mostly composed of imperfect hexagonal carbon rings without long-range ordering. These unsaturated bonds can facilitate a strong interaction with Na atoms and thus can act as catalytic sites for Na plating. Following this logic, Yun *et al.* designed microporous catalytic carbon nanotemplates (MC-CNTs) with various density of defects by tuning heating temperature.[44] The experimental data reveals that the MC-CNTs prepared at 800 ^oC (MC-CNT-800) have a much lower overpotential due to more defective sites, but experiences a large decay in Faradaic efficiency after around 200 cycles (Figure 11a, b). This can be explained by the fact that the abundant defects can induce Na aggregation and therefore the passivation film is formed on the active carbon surface. In comparison, a higher-temperature processed MC-CNTs at 2400 ^oC (MC-CNT-2400) managed to maintain 99.9% Coulombic efficiency over 1000 cycles, which can be attributed to its distinctive graphitic structure (Figure 11c, d). Hence, defective and graphitic degree are both key factors to

enable stable and long-cycle life Na metal anodes. In conjunction with the advantages of dopants, rich defects and large specific surface area of carbon networks, Huang *et al.* constructed N, S co-doped hollow carbon fibers (D-HCF) as sodiophilic hosts to provide abundant preferential nucleation sites that enable homogenous Na deposition (Figure 11e-i).[45] Furthermore, the superiority of D-HCF electrode is further demonstrated in a full cell with $Na_3V_2(PO_4)_3$ as cathode, which can deliver a stable discharge capacity with an average Coulombic efficiency of over 99% and superior rate capability.

Meanwhile, Mitlin's group employed graphene layers with tuned structures and chemistry as substrate to examine the role of graphene defects on Na plating.[46] With a novel directional flow-aided sonochemistry exfoliation technique (Figure 12a), graphite is exfoliated into graphene layers that are either nearly defect free (at-edge sonication graphene, AES-G) or highly defective (in-plane sonication graphene, IPS-G). AES-G and IPS-G have a Raman G/D band intensity ratio of 14.3 and 1.6, respectively, indicating that AES-G is highly ordered while IPS-G is highly disordered (Figure 12b). This study revealed that the graphene defects can be detrimental for Na plating and stripping as they catalyze SEI formation, leading to an unstable and thick SEI film (Figure 12c). As a result, the AES-G cell exhibits an average Coulombic efficiency of nearly 100% over 100 cycles, while the IPS-G electrode shows an unstable Coulombic efficiency due to Na dendrite formation (Figure 12d). Correspondingly, a smooth surface can be observed on AES-G after 100 cycles. In comparison, the IPS surface is quite rough, indicative of Na dendrite growth (Figure 12e, f). Likewise, the overpotential of APS-G electrode can remain stable throughout cycling, whereas severe voltage fluctuations are presented in the voltage profile of IPS-G due to unstable SEI growth and an associated unstable Na metal (Figure 12g). Therefore, further studies on the role of defect in carbon substrates for Na plating are needed.

5.2.4 Physical Implantation of Nucleation Seeds

The strategies described above demonstrate that functional groups, dopants or defects can increase the substrate affinity with Na atoms and reduce Na nucleation energy barrier, therefore contributing to homogenous Na plating without Na dendrite growth. However, the graphitization and electronic conductivity can be potentially sacrificed, and this can lead to a high interface resistance and large polarization especially during relatively high rate cycling. Additionally,

random Na nucleation behavior makes it rather difficult to confine Na nucleation and deposition within the 3D networks, resulting in Na dendrite formation. Anchoring heterogenous seeds that can react with Na to form alloys can improve the wettability with Na, thus directing Na nucleation at specific sites for controllable morphology. Based on this rationale, a series of metallic species including nanoparticles, metal cations, clusters, single atoms have been proposed as seeds for Na heterogenous nucleation. Through this way, the underlying substrate becomes highly sodiophilic, which can increase the critical nuclei size and lower the nucleation overpotential.

Yang *et al.* found that alkaline earth metals including Be, Mg and Ba foil have adequate solubility in Na metal to form solid solution surface layers,[47] which can serve as buffer layers to effectively reduce Na nucleation barriers and guide facile Na nucleation (Figure 13a). With the merits of stability and non-toxicity, Mg clusters can be homogenously dispersed into a 3D conductive hierarchical structure (3DHS) as heterogenous seeds to further eliminate the Na nucleation barrier (Figure 13b, c). As a result, a dendrite-free Na metal anode with minimal volume change and superior cycling stability up to 1350 hours can be realized (Figure 13d, e).

Because of the preferential alloying reaction, Sn-based materials are the most promising alloy-type anodes for Na metal anode. In this context, Li *et al.* presented a facile and scalable approach to synthesize Sn nanoparticles (NPs) that are uniformly embedded within conductive and porous carbon network (denoted as Sn@C composite) to enable highly reversible and high-capacity Na metal anodes (Figure 14a).[48] The well-dispersed Sn NPs can serve as preferential nucleation sites to direct Na nucleation due to the alloying reaction between Na and Sn, thus lowering the Na nucleation barrier and contributing to uniform Na plating (Figure 14b). Meanwhile, the carbon network can act as buffer layer to effectively minimize the volume change and alleviate the exfoliation of Sn NPs over long-term cycles. Benefiting from its unique structure and the synergistic effect of Sn NPs and carbon matrix, the as-prepared Sn@C composite can enable highly reversible and dendrite-free Na metal anodes with a high average Coulombic efficiency of 99.3% and a consistently low voltage hysteresis of around 30 mV over 1250 hours at a current density of 2 mA cm^{-2} and a high capacity of 5 mAh cm^{-2} (Figure 14c). Furthermore, a room-temperature Na-S full cell with commercial Na_2S powder as cathode and Sn@C composite/Na metal as anode can exhibit a high and stable discharge capacity at 1 A g^{-1} with an average Coulombic efficiency of 96.2% over 100 cycles. The discharge capacity and rate

capability are far more superior compared to those using bare Na metal anode and Cu/Na anode, further demonstrating the high reversibility of modified Na metal anode in affecting the full cell performance. Notably, the Na-S cell only contains 1 mAh cm^{-2} of Na deposit, which can avoid excessive Na metal usage and therefore present an effective strategy to enable stable, safe and cost-effective Na metal batteries.

Besides carbon hosts, MXene as a new family of 2D materials with tunable interlayer spacing can act as a promising host material for Na metal. To endow the hosts with high Na wettability and large interlayer gap to accommodate the deposited Na, intercalated cationic surfactants was first used to increase the interlayer spacing followed by subsequent Sn^{2+} intercalation, achieving Sn (II) pillared Ti_3C_2 MXene (Figure 14d).[49] Based on this design, Na can preferentially nucleate around the Sn (II) seeds and then forms Na–Sn alloy by alloying reaction. Consequently, the thermodynamic barrier for Na nucleation can be greatly reduced and thus present a lower nucleation overpotential at varied current densities (Figure 14e). Due to a high interaction force, Na ions continue to deposit around the formed alloys within the MXene, thus contributing to the uniform Na deposition without dendrites. As a result, highly stable Na composite anodes can be realized at a high current density up to 10 mA cm^{-2} and a high capacity of 5 mAh cm^{-2} over 500 cycles in ether-based electrolyte (Figure 14f). Furthermore, the full cell using MXene-based Na metal composite anode coupled with $Na_3V_2(PO_4)_3$ cathode exhibits superior electrochemical performance than that using host-less commercial Na metal anode.

Among all kinds of metallic species, single atoms can potentially maximize the atomic utilization efficiency and provide rich actives sites. Thus, Yan *et al.* homogenously dispersed N-anchored zinc (Zn) single atoms on the surface of N-doped carbon substrates (Zn_{SA}-N-C) to direct the Na heterogeneous nucleation and spontaneously regulate Na deposition with spatial and structural control (Figure 15a).[50] Likewise, the anchored Zn single atoms can react with Na to form $NaZn_x$ alloy phases, enabling the Zn_{SA}-N-C substrate to have an excellent affinity and strong interaction with Na ions, which can provide abundant sodiophilic sites for Na nucleation and thus enable a low nucleation overpotential (Figure 15b, c). Consequently, a high Coulombic efficiency of 99.8% over 350 cycles and a stable cycling behavior with constantly low voltage hysteresis can be achieved (Figure 15d). Moreover, a high Na utilization of nearly 100% in full cells can be realized. More importantly, full cells composed of Zn_{SA}-N-C with limited Na resources as anode and $Na_3V_2(PO_4)_3$ as cathode can deliver a stable specific capacity with

Coulombic efficiency of around 100% over 1000 cycles, further demonstrating the advantages of using of Zn_{SA}-N-C electrodes. Based on the above discussions, Table 2 summarizes the works on the development of different metals as sodiophilic sites for Na nucleation or 3D matrices that can effectively reduce Na nucleation barriers to improve electrochemical performance. Evidently, most studies have been conducted in ether electrolytes. In comparison, conventional carbonate electrolytes have greater industrial compatibility due to wider electrochemical stability window and lower volatility. Hence, future studies on nucleation overpotential should focus on carbonate electrolytes for more industrial relevant applications.

Table 2. Comparison of different metals in stabilizing Na metal anodes

Work	Metal	Mechanism	Electrolyte	Nucleation Overpotential	Cycling condition	Average Coulombic efficiency	Overpotential	Advantage
31	porous Al	3D matrix	ether	—	1 mA/cm^2; 0.5 mAh/cm^2	99.8% over 1000 cycles	~20 mV	Cheap
32	Ag nanopaper	3D matrix	ether	—	1 mA/cm^2; 1 mAh/cm^2	~100% over 400 cycles	~20 mV over 800 h	Light but expensive
37	Functional Cu foam	3D sodiophilic matrix	carbonate	—	2 mA/cm^2; 3 mAh/cm^2	—	~120 mV over 300 h	Commercial but heavy
29,30	Au film on Cu	Alloying reaction to improve sodiophilicity	ether	0 mV at 0.05 mA /cm^2	2 mA/cm^2; 1 mAh/cm^2	~99.8% over 500 cycles	—	Expensive
30	Sn Nanoparticles			~10 mV at 0.05 mA /cm^2	2 mA/cm^2; 1 mAh/cm^2	~99.9% over 2000 cycles	0.1 mV	Cheap but with volume change
	Sb Nanoparticles			~10 mV at 0.05 mA /cm^2		~99.9% over 1700 cycles	0.1 mV	
47	Mg clusters in 3D carbon			6.6 mV at 0.05 mA /cm^2	0.5 mA/cm^2; 1 mAh/cm^2	—	~27mV over 1350 h	Low overpotential with negligible volume change
48	Sn nanoparticles in 3D carbon	3D matrix with nucleation seed	ether	~20 mV at 2 mA /cm^2	2 mA/cm^2; 5 mAh/cm^2	~99.3% over 250 cycles	—	Cheap, high reversibility with negligible volume change
49	Sn (II) in 3D MXene			~40 mV at 4 mA /cm^2	4 mA/cm^2; 3 mAh/cm^2	~99.3% over 300 cycles	35 mV at 5 mA/cm^2 and 3 mAh/cm^2 over 200 h	High reversibility with negligible volume change
50	Zn single-atoms in 3D carbon			0 mV	0.5 mA/cm^2; 0.5 mAh/cm^2	~99.8% over 350 cycles	~50 mV at 1 mA/cm^2 and 1 mAh/cm^2 over 350 h	High utilization, low overpotential with negligible volume change

6. Concluding Remarks and Perspectives

Na metal is the most promising alternative to Li metal as an anode for the next-generation battery systems due to its high theoretical capacity, low electrochemical potential, as well as low cost and high natural abundance of Na resources. Nevertheless, in order to efficiently protect Na metal anode from unstable SEI formation and dendrite growth, there is still a lack of in-depth theoretical and experimental investigations to fully understand the relevant mechanisms.

Uncontrolled Na dendrite growth can induce severe safety concern, which should stand at the forefront of battery technology. Manipulating Na nucleation at specific sites to direct Na deposition for dendrite-free Na metal anodes is necessary. The research on Na deposition is still in its infancy due to the lack of powerful in situ/operando characterization techniques to understand the initial plating behavior and Na dendrite formation process. In addition, SEI components and structures can significantly impact Na^+ transport and diffusion pathways and therefore affecting the Na nucleation behaviors. However, a detailed understanding related to Na SEI components and structures is still missing. Also, the influence of SEI breakage upon deposition should be taken into consideration. Most studies conducted to date are results-oriented, relying on the final results to draw scientific insights. However, it is even more important to make close connection between experiments and theories in an iterative manner in order to gain fundamental framework. Therefore, in-depth computational and in-situ experimental studies in terms of Na nucleation and plating are imperative for comprehensive understanding on Na nucleation process mechanism.

With the promising potentials of Na-based batteries, there are already a handful of companies such as Natron Energy, Faradion, and AGM Batteries working to commercialize the technology. However, although significant progress has been made on interface engineering and solid electrolyte development for enabling Na-based batteries with stable cycling performance, most of the researches conducted to date were tested on relatively low current densities and areal capacities, as well as low active material mass loading. In order to realize practical energy storage solutions, it is necessary to devote some of the research focus to developing new cell chemistries that can sustain real world requirements in terms of applied current density and ramp rate. Also, those effective solutions for suppressing Na metal dendrite oftentimes required costly materials or expensive experimental procedure. Therefore, it is worthwhile to develop new strategies with the specific aim of driving down the costs of implementation in order to bring significant research findings out to the world.

Liquid electrolyte modification can be a practical near-term solution to resolve the challenges with Na dendrite as it is a straightforward method that can be readily implemented into the existing manufacturing procedure. Most studies involving Na nucleation regulations are limited in ether-based electrolytes, as they can deliver relatively more superior Na metal batteries performance, but it is rarely used in the industry due to its more flammable nature than that of

carbonate electrolyte. The electrolyte composition variations can profoundly influence the Na^+ transport pathway and thus lead to a different nucleation process and deposition morphology. Compared to ether-based electrolyte, traditional carbonate-based electrolyte that possesses wider electrochemical window, lower volatility, and is more industrially compatible. Generally, it is more challenging to realize uniform Na deposition in carbonate electrolytes due to the more fragile SEI formation. Additive in carbonate electrolyte shows promising results, but more rigorous tests under various industrial standard conditions are needed to quantify the performance in real world situations. Thus, more efforts need to be devoted to improving our understanding on Na nucleation mechanism and behavior in various electrolytes for dendrite-free Na metal anodes.

Sodiophilic 3D networks are the effective strategies to suppress Na dendrite growth and minimize volume expansion via synergistically regulating Na nucleation, but the SEI factor is often neglected. For these investigations on sodiophilic materials for Na metal, it is highly desirable to elucidate the relationship between physical property change and the chemical reactions on the Na metal with the corresponding dynamic SEI. It is necessary to integrate in-situ and operando investigations to monitor bulk Na and SEI structural evolution. Although highly promising, constructing a sodiophilic Na metal host or thin film coating onto Na metal anode can be very resource-intensive methods. Therefore, future research focus on this topic can be devoted to reducing the operating and material expenses. In order to lower the relevant cost, it is necessary to improve the instrumental technology that can provide facile and consistent artificial SEI coating as well. Overall, sodiophilic host and SEI formation can be the longer-term solution towards safe Na metal batteries.

Lastly, solid electrolytes can be the ultimate solution for a safe Na metal anode by replacing the flammable organic liquid electrolyte. Solid electrolyte shows great promise in improving battery safety due to its non-flammable property and ability to mechanically suppress Na dendrite growth. But the low ionic conductivity of solid electrolyte and its poor wettability with Na metal anodes result in unsatisfying performance that lags far behind that of liquid electrolyte. The high interfacial impedance of solid electrolytes makes it challenging to achieve homogenous Na deposition that can further deteriorate the interface stability and ultimately lead to a high voltage hysteresis. Also, dendrite growth on solid/solid interface as well as inside solid electrolytes can still be observed due to the poor contact between solid electrolytes and Na metal

anode that leaves room for dendrite growth. Meanwhile, insufficient compactness and low bulk density with void spaces in solid electrolytes, and the ionic conductivity difference between grain and grain boundary can also lead to dendrite formation. Therefore, the future development of solid-state Na batteries should incorporate the Na nucleation regulation to enable uniform deposition between the multiphase solid interfaces. As one of the most promising energy storage systems, there is still a long way to go in realizing the practical applications of Na metal batteries based on the requirements of safety, energy density and efficiency.

Conflicts of interest

There are no conflicts to declare.

Acknowledgements

The authors greatly acknowledge the support from Young Investigator Program funded by U.S. Air Force Office of Scientific Research under award FA9550-17-1-0184, as well as the support from the start-up funds at Thayer School of Engineering, Dartmouth College.

References

1. Z. Yang, J. Zhang, M. C. W. Kintner-Meyer, X. Lu, D. Choi, J. P. Lemmon and J. Liu*, Chem. Rev.* 2011, **111**, 3577-3613.

2. C. Vaalma, D. Buchholz, M. Weil and S. Passerini, *Nat. Rev. Mater.* 2018, **3**, 18013.

3. J-Y. Hwang, S-T. Myung and Y-K. Sun, *Chem. Soc. Rev.,* 2017, **46**, 3529.

4. X. Xiang, K. Zhang and J. Chen, *Adv. Mater,* 2015, **27**, 5343-5364.

5. M. S. Islam and C. A. J. Fisher, *Chem. Soc. Rev.* 2014, **43**, 185-2014.

6. B. Lee, M. Kim, S. Kim, J. Nanda, S. J. Kwon, H. D. Jang, D. Mitlin and S. W. Lee. *Adv. Energy* Mater. DOI: 10.1002/aenm.201903280.

7. Y. Liu, B. V. Merinov and W. A. Goddard III, *PNAS* 2016, **113**, 3735-3739.

8. B. Lee, E. Paek, D. Mitlin and S. W. Lee, *Chem. Rev***.** 2019, **119**, 5416-5460.

9. Y. Zhao, K. R. Adair and X. Sun, *Energy Environ. Sci.* 2018, **11**, 2673.

10. E. Matios, H. Wang, C. Wang and W. Li, *Ind. Eng. Chem. Res.* 2019, **58**, 9758-9780.

11. H. Liu, X-B, Cheng, Z. Jin, R. Zhang, G. Wang, L-Q. Chen, Q-B, Liu, J-Q, Huang and Q. Zhang, *EnergyChem,* 2019, **1**, 100003.

12. M. Okoshi, Y. Yamada, A. Yamada and H. Nakai, *J. Electro. Soc.* 2013, **160**, A2160-A2165.

13. Y-S. Hong, N. Li, H. Chen, P. Wang, W. Song, D. Fang, *Energy Storage Materials*, 2018, **11**, 118-126.

14. Y. Deng, J. Zheng, A. Warren, J. Yin, S. Choudhury, P. Biswal, D. Zhang and L. A. Archer, *Adv. Energy Mater.* 2019, **9**, 1901651.

15. M. Han, C. Zhu, T. Ma, Z. Pan, Z. Tao and J. Chen, *Chem. Commun.,* 2018, **54**, 2381.

16. P. M. Bayley, N. M. Trease and C. P. Grey, *J. Am. Chem. Soc.* 2016, **138**, 1955-1961.

17. A. Mashreghi, H. Zare, *Curr Appl Phys*. 2016, **16**, 599-604.

18. M. R. Khelladi, L. Mentar, A. Azizi, F. Kadirgan, G. Schmerber and A. Dinia, *Appl Surf Sci.* 2012, **258**, 3907-3912.

19. D. R. Ely and R. E. García, *J. Electro. Soc.* 2013, **160**, A662-A668.

20. B. J. L. Barton, J. O'M. Bockeris, *Proc. R. Soc. London, Ser. A* 1962, **268**, 485-505.

21. B. Scharifker and G. Hills, *Electrochim. Acta* 1983, **28**, 879-889.

22. Y-J. Kim, J. Lee, S. Yuk, H. Noh, H. Chu, H. Kwack, S. Kim, M-H. Ryou and H-T. Kim, *J. Power Sources* 2019, **438**, 227005.

23. M. Jäckle and A. Groß, *J. Chem. Phys.* 2014, **141**, 174710.

24. S. Choudhury, S. Wei, Y. Ozhabes, D. Gunceler, M. J. Zachman, Z. Tu, J. H. Shin, P. Nath, A. Agrawal, L. F. Kourkoutis, T. A. Arias and L. A. Archer, *Nat. Commun.* 2017, **8**, 88.

25. V. Laurent, D. Chatain and N. Eustathopoulos, *Materials Science and Engineering, A* 1991, **A135,** 89-94.

26. J. Wang, H. Wang, J. Xie, A. Yang, A. Pei, C-L. Wu, F. Shi, Y. Liu, D. Lin, Y. Gong and Y. Cui, *Energy Storage Materials*, 2018, **14**, 345-350.

27. A. P. Cohn, N. Muralidharan, R. Carter, K. Share and C. L. Pint, *Nano Lett.* 2017, **17**, 1296-1301.

28. X. Hu, P. H. Joo, H. Wang, E. Matios, C. Wang, J. Luo, X. Lu, K. Yang and W. Li, *Adv. Funct. Mater.* 2019, **29**, 1807974.

29. S. Tang, Z. Qiu, X-Y. Wang, Y. Gu, X-G. Zhang, W-W. Wang, J-W. Yan, M-S. Zheng, Q-F. Dong and B-W. Mao, *Nano Energy* 2018, **48**, 101-106.

30. S. Tang, Y-Y. Zhang, X-G. Zhang, J-T. Li, X-Y. Wang, J-W. Yan, D-Y. Wu, M-S. Zheng, Q-F. Dong and B-W. Mao, *Adv. Mater.* 2019, **31**, 1807495.

31. S. Liu, S. Tang, X. Zhang, A. Wang, Q-H. Yang and J. Luo, *Nano Lett.* 2017, **17**, 5862-5868.

32. Z. Wang, X. Zhang, S. Zhou, K. Edström, M. Strømme and L. Nyholm, *Adv. Funct. Mater.* 2018, **28**, 1804038.

33. W. Luo, Y. Zhang, S. Xu, J. Dai, E. Hitz, Y. Li, C. Yang, C. Chen, B. Liu and L. Hu, *Nano Lett.* 2017, **17**, 3792-3797.

34. S-S. Chi, X-G. Qi, Y-S. Hu and L-Z. Fan, *Adv. Energy Mater.* 2018, **8**, 1702764.

35. W. Go, M-H. Kim, J. Park, C.H. Lim, S. H. Joo, Y. Kim and H-W. Lee, *Nano Lett*. 2019, **19**, 1504-1511.

36. Q. Zhang, Y. Lu, M. Zhou, J. Liang, Z. Tao and J. Chen, *Inorg. Chem. Front.* 2018, **5**, 864.

37. C. Wang, H. Wang, E. Matios, X. Hu and W. Li, *Adv. Funct. Mater.* 2018, **28**, 1802282.

38. X. Ma, Y. Gu, Y. Yao, H. Jin, X. Zhao, X. Yuan, Y. Lian, P. Qi, R. Shah, Y. Peng and Z. Deng, *J. Mater. Chem. A*, 2019, **7**, 20926.

39. A. Wang, X. Hu, H. Tang, C. Zhang, S. Liu, Y-W. Yang, Q-H. Yang and J. Luo, *Angew. Chem. Int. Ed.* 2017, **129**, 12083-12088.

40. P. Liu, Y. Wang, Q. Gu, J. Nanda, J. Watt and D. Mitlin. *Adv. Mater.* 2020, **32**, 1906735.

41. L. Ye, M. Liao, T. Zhao, H. Sun, Y. Zhao, X. Sun, B. Wang and H. Peng, *Angew. Chem. Int. Ed.* 2019, **58**, 2-9.

42. B. Sun, P. Li, J. Zhang, D. Wang, P. Munroe, C. Wang, P. H. L. Notten and G. Wang, *Adv. Mater.* 2018, **30**, 1807495.

43. Y. Zhao, X. Yang, L-Y. Kuo, P. Kaghazchi, Q. Sun, J. Liang, B. Wang, Andrew Lushington, R. Li, H. Zhang and X. Sun, *Small* 2018, **14**, 1703717.

44. H. J. Yoon, N. R. Kim, H-J. Jin and Y. S. Yun, *Adv. Energy Mater.* 2018, **8**, 1701261.

45. X. Zheng, P. Li, Z. Cao, W. Luo, F. Sun, Z. Wang, B, Ding, G. Wang and Y. Huang, *Small,* 2019, **15**, 1902688.

46. W. Liu, P. Li, W. Wang, D. Zhu, Y. Chen, S. Pen, E. Paek and D. Mitlin, *ACS Nano* 2018, **12**, 12255-12268.

47. M. Zhu, S. Li, B. Li, Y. Gong, Z. Du and S. Yang, *Sci. Adv.* 2019, **5**, eaau6264.

48. H. Wang, E. Matios, C. Wang, J. Luo, X. Lu, X. Hu, Y. Zhang and W. Li, *J. Mater. Chem. A*, 2019, **7**, 23747.

49. J. Luo, C. Wang, H. Wang, X. Hu, E. Matios, X. Lu, W. Zhang, X. Tao and W. Li, *Adv. Funct. Mater.* 2019, **29**, 1805946.

50. T. Yang, T. Qian, Y. Sun, J. Zhong, F. Rosei and C. Yan, *Nano Lett.* 2019, **11**, 7827-7835.

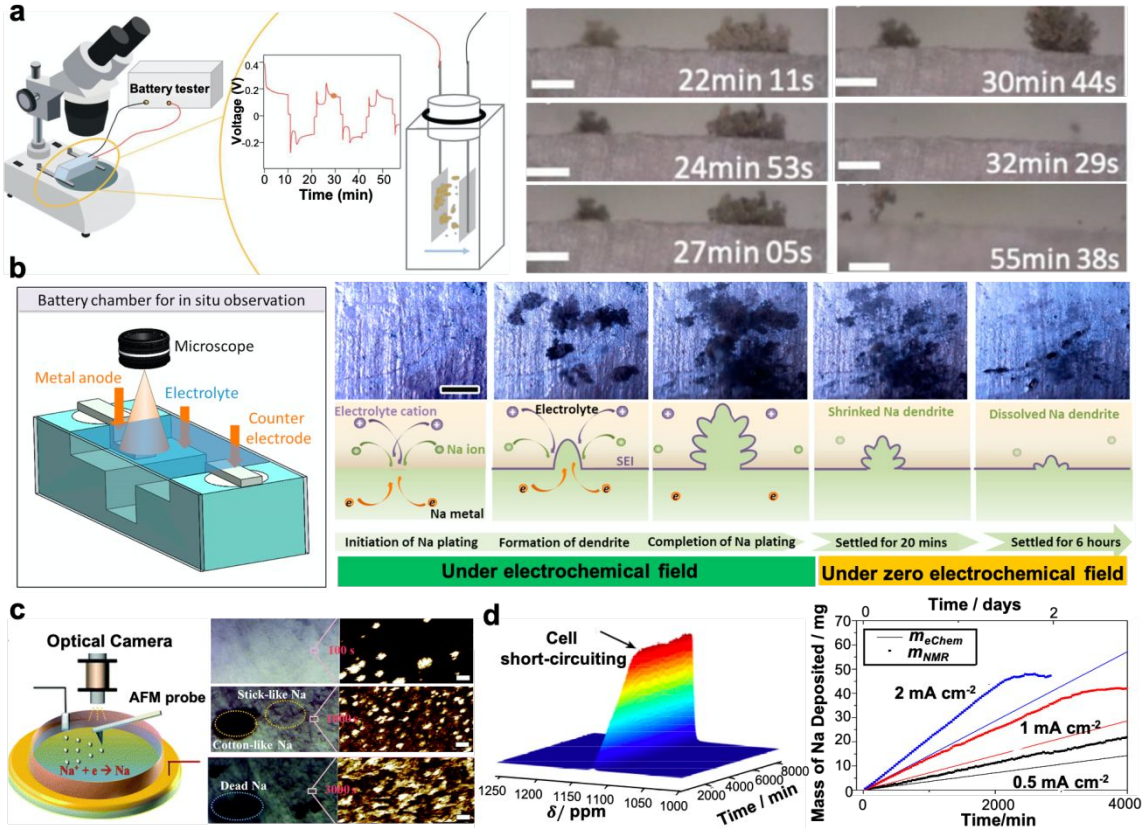

Figure 1. Different in-situ techniques to monitor Na deposition process. (a) Schematic illustration of in-situ visualization experiment setup and corresponding snapshots of videos collected at different time points during galvanostatic plating and stripping process. Reproduced with permission.[14] Copyright 2019, Wiley-VCH. (b) Schematic of battery chamber for in-situ optical observation on Na metal anode surface and Na dendrite changes during the plating process and subsequent settling. Scale bar: 1 mm. Reproduced with permission.[13] Copyright 2018, Elsevier Ltd. (c) Schematic of in-situ AFM setup (left) for testing Na deposition with in-situ optical images (middle) and AFM height images (right) during Na plating. Scale bars: 1 μm. Reproduced with permission.[15] Copyright 2019, Royal Society of Chemistry. (d) In-situ ^{23}Na NMR spectroscopy for quantifiable measurement of Na microstructure amounts. Reproduced with permission.[16] Copyright 2016, American Chemical Society.

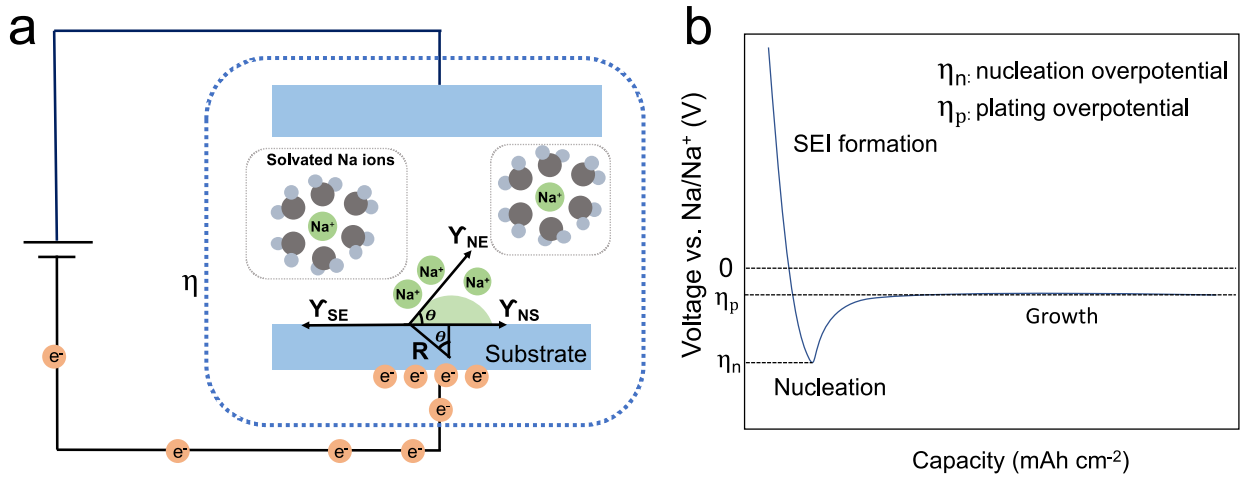

Figure 2. (a) Schematic for Na heterogenous nucleation on the current collector (substrate) under an electric field. The Na nuclei radius (R) and overpotential (η), contact angle (Θ) and interface energy: γ_{SE} (substrate surface energy), γ_{NS} (nuclei surface energy), γ_{NE} (nuclei/electrolyte interfacial energy); as well as solvated Na ions are indicated. (b) Typical voltage profile of galvanostatic Na deposition in the first cycle. The corresponding process of SEI formation, nucleation and growth during Na deposition are marked.

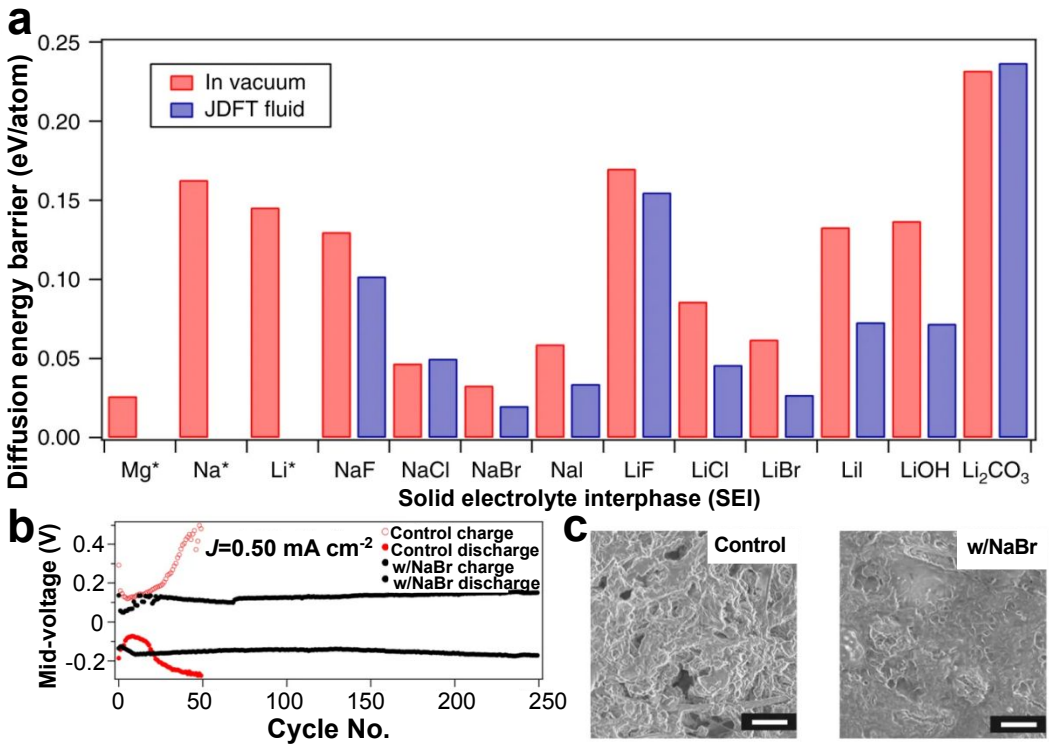

Figure 3. (a) Calculated diffusion energy barrier for Na ions transport on different surfaces. (b) Voltage hysteresis represented by the mid-voltage values during charging and discharging cycles for NaBr coated and control Na cells at 0.5 mA cm^{-2}. (c) Morphology comparison of bare Na metal as control group and NaBr-coated Na metal after cycling. Scale bars: 5 μ m. Reproduced with permission.[24] Copyright 2017, Nature Publishing Group.

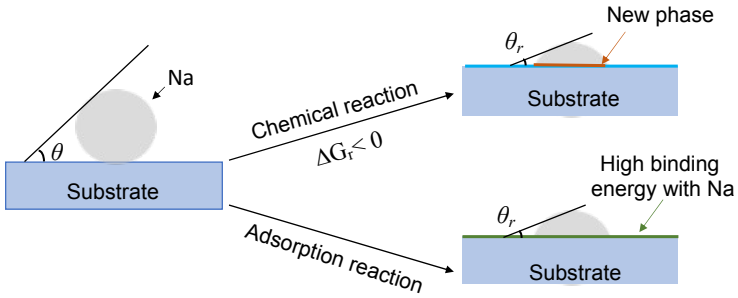

Figure 4. Schematic illustrating the effect of interface property on Na wettability through chemical reaction or adsorption reaction.

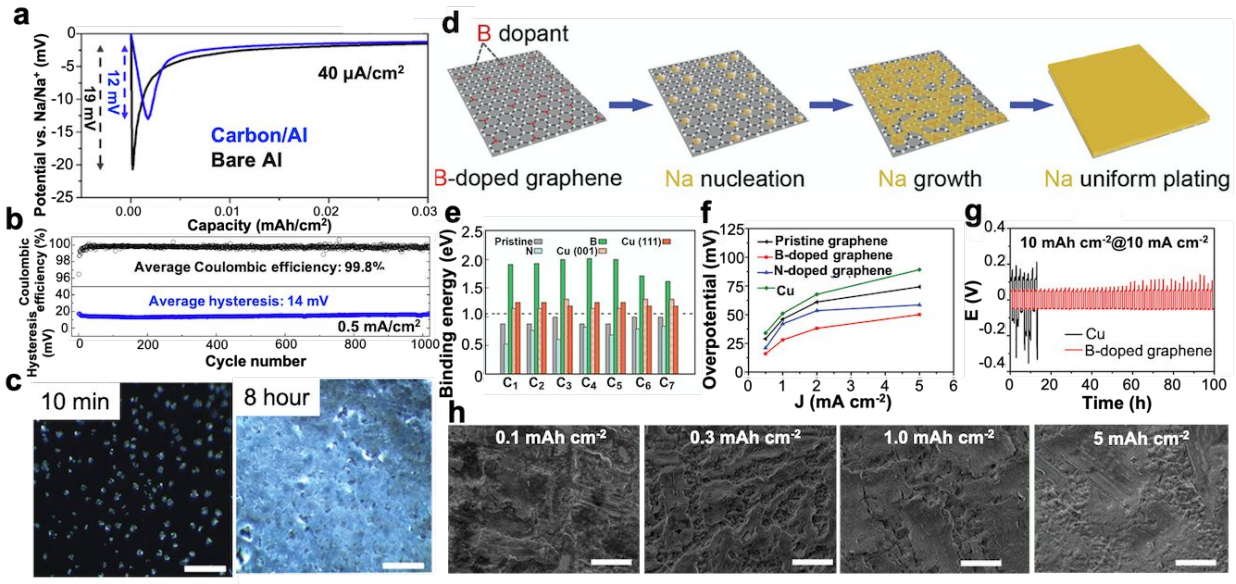

Figure 5. (a) Galvanostatic voltage profiles of Na plating on carbon/Al and bare Al at 40 μA cm^{-2} to compare the nucleation overpotential. (b) Voltage efficiency and voltage hysteresis of Na plating and stripping on carbon/Al current collector at 0.5 mA cm^{-2} and 0.25 mAh cm^{-2}. (c) Morphology evolution of Na deposition on carbon/Al current collector. Scale bars: 500 μm. Reproduced with permission.[27] Copyright 2016, American Chemical Society. (d) Schematic of Na nucleation, growth and subsequent plating process on B-doped graphene film. (e) Calculated binding energies of Na metal with different substrates. (f) Plots of nucleation overpotentials for Na deposition on pristine graphene, B-doped graphene, N-doped graphene and Cu substrate as current densities, respectively. (g) Voltage-time profiles of Na plating and stripping in symmetric cells made from Na/Cu and Na/B-doped graphene electrodes, respectively. (h) Morphology evolution of deposited Na on B-doped graphene at various plating capacities. Scale bars: 20 μm. Reproduced with permission.[28] Copyright 2019, Wiley-VCH.

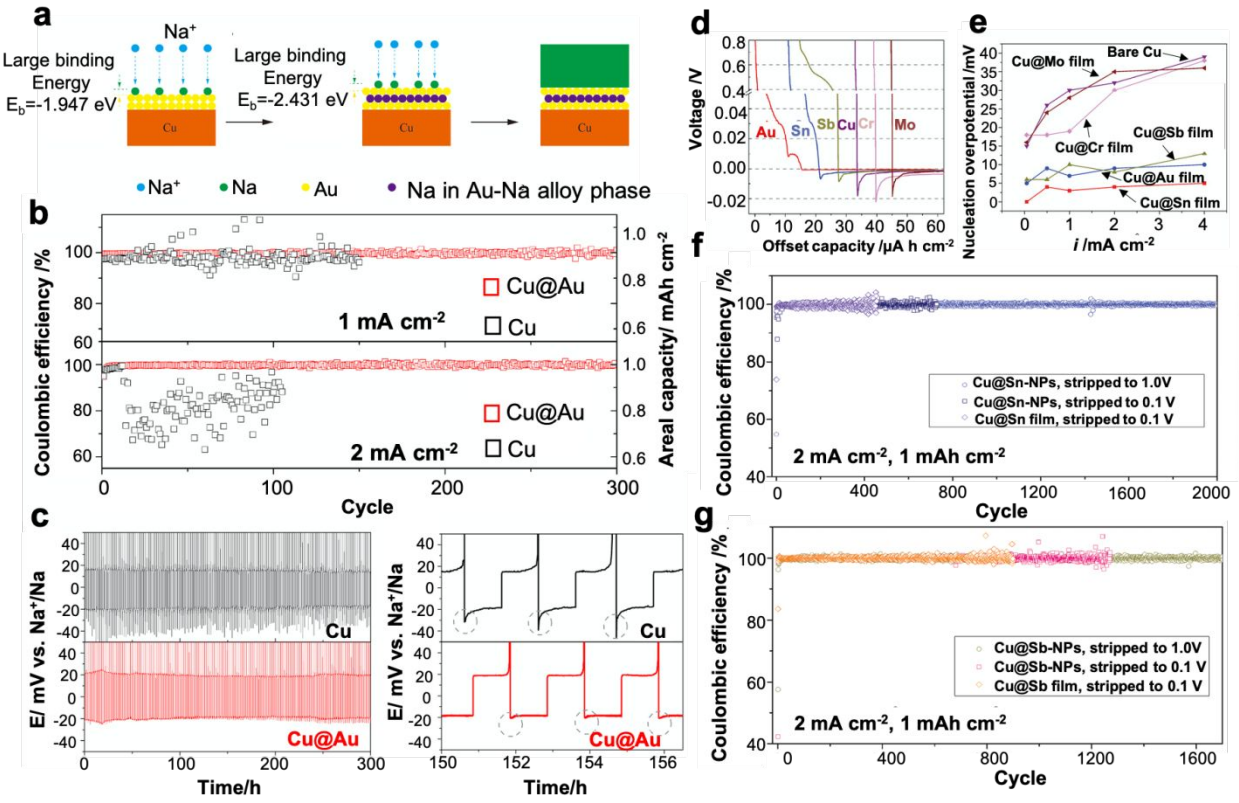

Figure 6. (a) Schematic showing Na plating process on Cu@Au substrate. (b) Coulombic efficiencies of Na plating and stripping on Cu and Cu@Au substrates with 1 mAh cm^{-2} at 1 mA cm^{-2} and 2 mA cm^{-2}. (c) Corresponding voltage profiles at 1 mAh cm^{-2}. Reproduced with permission.[29] Copyright 2018, Elsevier Ltd. (d) Voltage profiles of Na plating/stripping on Au, Sn, Sb, Cu, Cr and Mo, respectively. (e) Plots of nucleation overpotentials of Na deposited on Cu@Au film, Cu@Sb film, Cu@Sb film, bare Cu, Cu@Cr film and Cu@Mo film as function of current densities. (f) Coulombic efficiencies of Na plating and stripping cycles on Cu@Sn-NPs and Cu@Sn film at 2 mA cm^{-2} and 1 mAh cm^{-2} with cutoff potentials of 0.1 V and 1 V, respectively. (g) Coulombic efficiencies of Na plating and stripping cycles on Cu@Sb-NPs and Cu@Sb film at 2 mA cm^{-2} and 1 mAh cm^{-2} with cutoff potentials of 0.1 V and 1 V, respectively. Reproduced with permission.[30] Copyright 2019, Wiley-VCH.

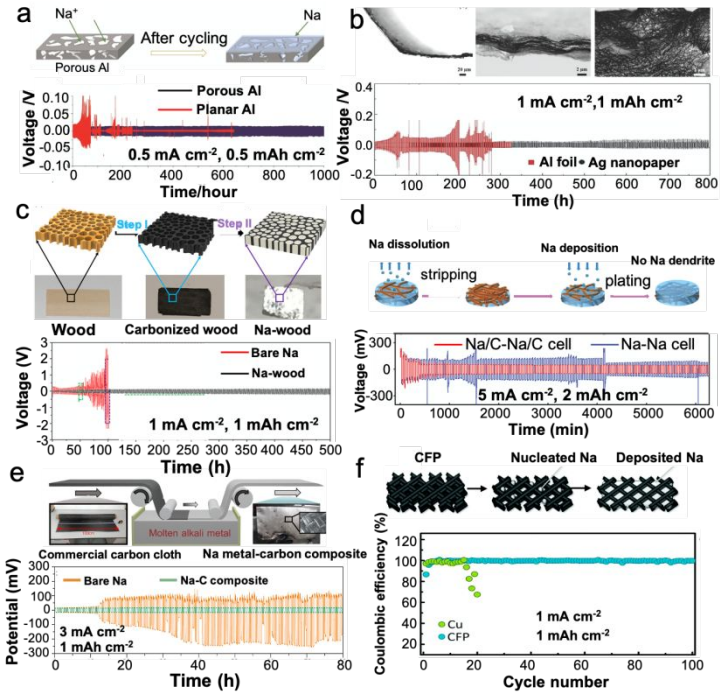

Figure 7. The implementation of various kinds of 3D hosts for dendrite-free Na metal anodes. (a) Schematic of Na deposition on Porous Al and galvanostatic cycling of symmetric Na@planar Al/Na and Na@porous Al/Na cells at 0.5 mA cm^{-2} and 0.5 mAh cm^{-2}. Reproduced with permission.[31] Copyright 2017, American Chemical Society. (b) Cross-section SEM image of Ag nanopaper and comparison of the cycling stabilities for the AgNP–Na|Na and Al–Na|Na cells at 1 mA cm^{-2} and 1 mAh cm^{-2}. Reproduced with permission.[32] Copyright 2017, Wiley-VCH. (c) Schematic of carbonization step and infusion of molten Na into carbonized wood as well as electrochemical performance of symmetric cells using Na-wood electrodes and bare Na metal electrodes at 1 mA cm^{-2} and 1 mAh cm^{-2}. Reproduced with permission.[33] Copyright 2017, American Chemical Society. (d) Schematic of Na infusion into carbon felt and comparison of the cycling stability of the Na/C composite and bare Na electrode symmetrical cell at 5 mA cm^{-2} and 2 mAh cm^{-2}. Reproduced with permission.[34] Copyright 2018, Wiley-VCH. (e) Schematic of Na infusion into nanocrevasse-rich carbon fibers and comparison of the cycling stabilities of the Na/carbon composite and bare Na electrode symmetrical cells at 3 mA cm^{-2} and 1 mAh cm^{-2}. Reproduced with permission.[35] Copyright 2019, American Chemical Society. (f) Schematic of Na nucleation and deposition into carbon fiber paper (CFP) as well as comparison of the Coulombic efficiency on Cu and CFP.[36] Copyright 2018, Royal Society of Chemistry.

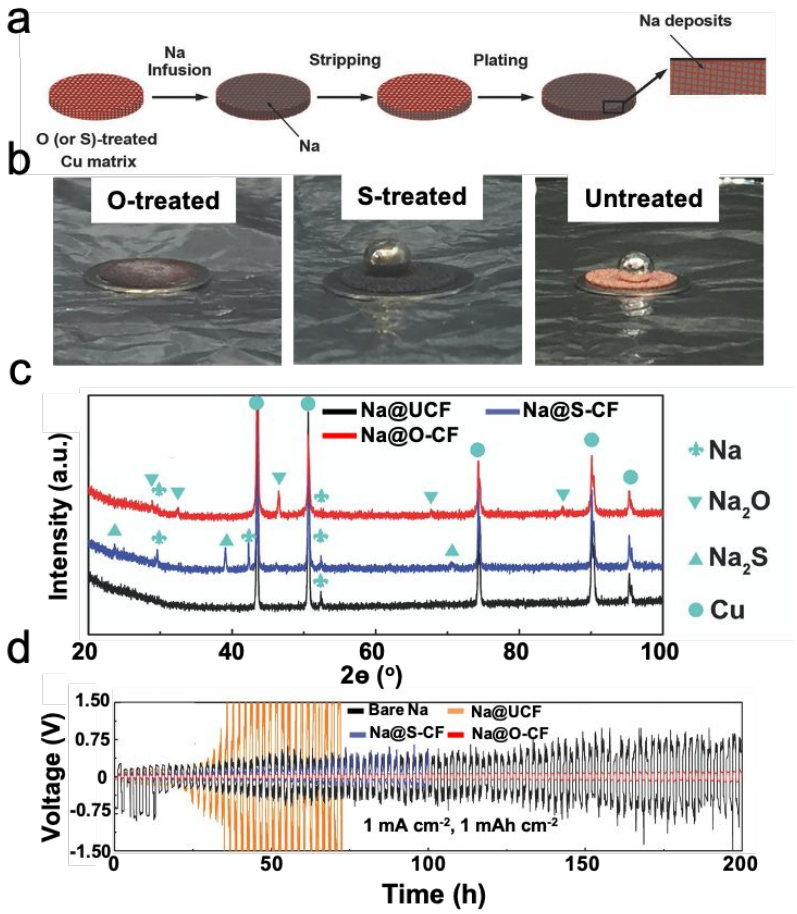

Figure 8. (a) Schematic illustration of infusing Na metal into surface-treated Cu matrix. (b) Comparison in the wettability of molten Na on (O, S-) treated vs. untreated Cu matrix. (c) XRD spectra of molten Na infusing into different kinds of matrices. O-treated, S-treated, and untreated Cu foams after infusion of molten Na are denoted by Na@O-CF, Na@S-CF, and Na@UCF, respectively. (d) Cycling performance of symmetric Na cells with different types of electrodes noted at 1 mA cm^{-2} and 1 mAh cm^{-2}. Reproduced with permission.[37] Copyright 2018, Wiley-VCH.

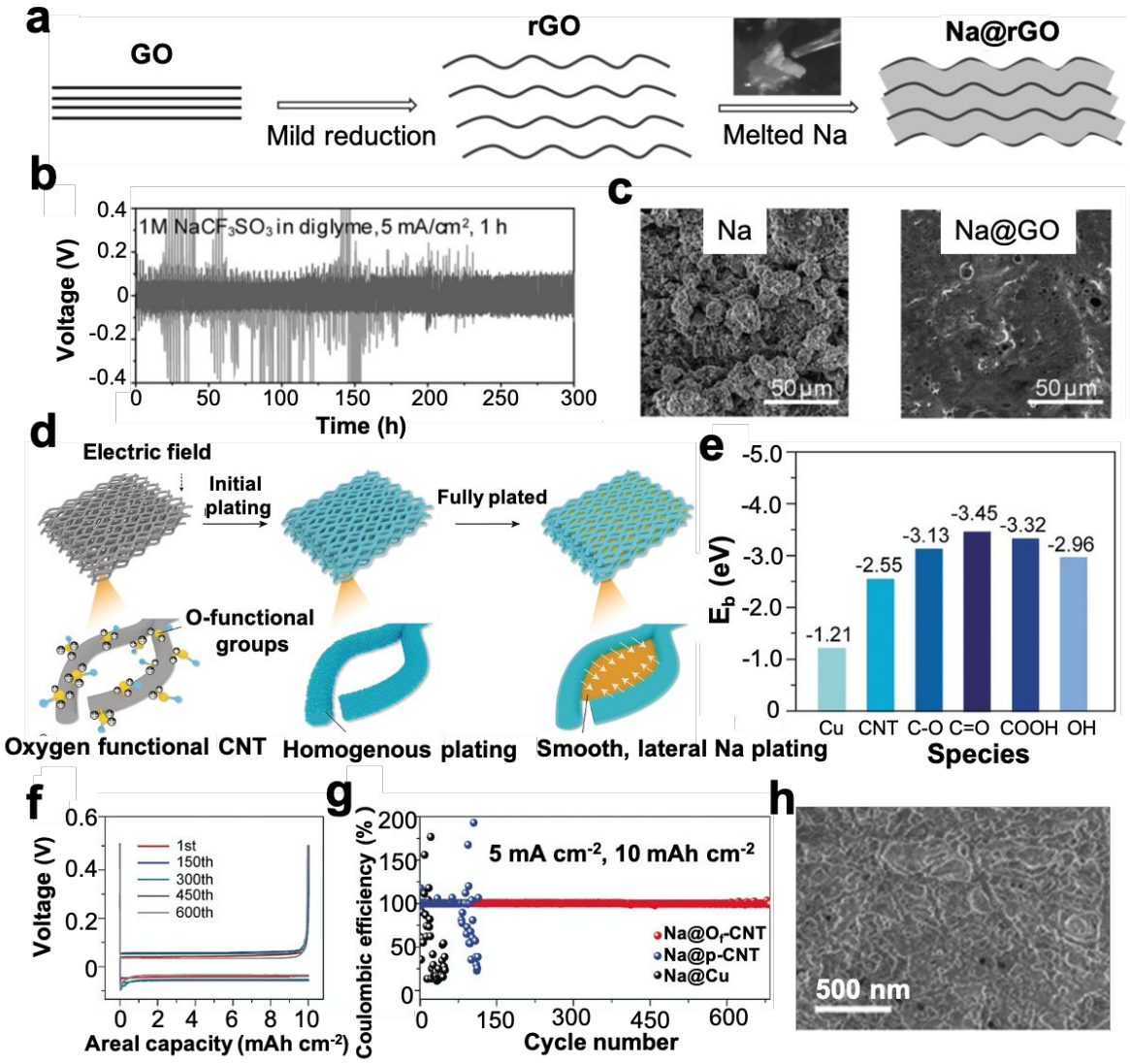

Figure 9. (a) Schematic representation for the preparation of Na@r-GO composites. (b) Galvanostatic cycling of symmetric Na/Na and Na@r-GO/Na@r-GO cells at 5 mA cm^{-2} and 5 mAh cm^{-2}. (c) SEM images of Na and Na@r-GO after 300 charge/discharge cycles. Reproduced with permission.[39] Copyright 2017, Wiley-VCH. (d) Schematic showing the Na deposition process on oxygen-functionalized carbon nanotube (O_f-CNT) networks. (e) Calculated binding energies of Na with different substrates noted. (f-g) Voltage profiles Na@O_f-CNT electrode at various cycles and corresponding Coulombic efficiencies of different electrodes at 5 mAh cm^{-2} and 10 mAh cm^{-2}. (h) SEM image of Na@O_f-CNT electrode with areal capacity of 10 mAh cm^{-2}. Reproduced with permission.[41] Copyright 2019, Wiley-VCH

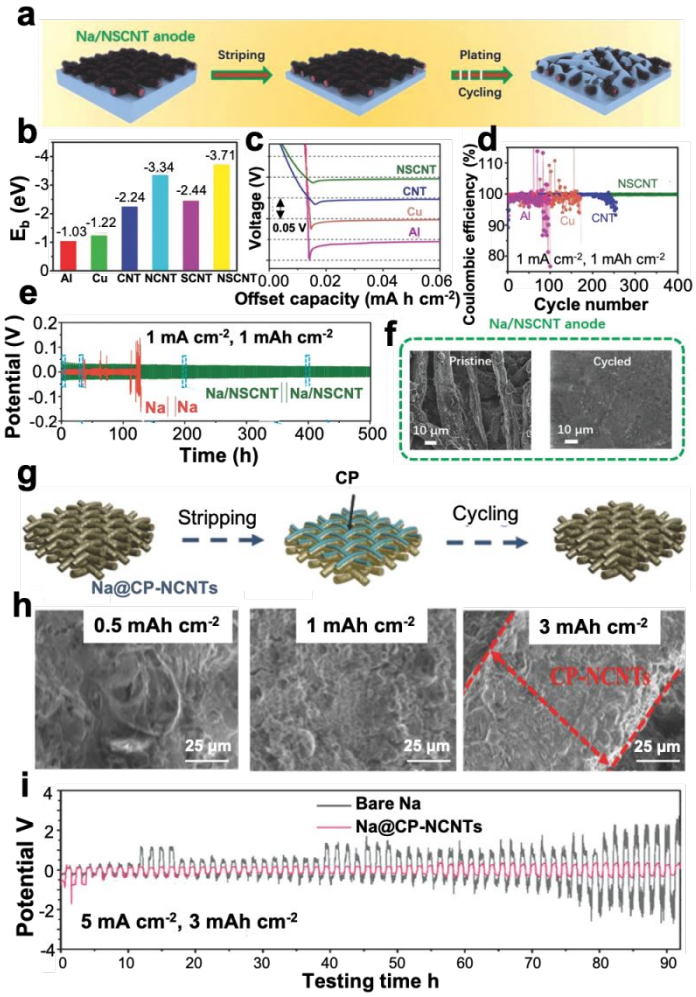

Figure 10. (a) Schematic of N, S co-doped nanotubes as interlayer for Na deposition. (b) Calculated binding energies of Na metal with different substrates. (c) The potential-capacity profiles during Na nucleation on different current collectors at 0.05 mA cm^{-2}. (d) Coulombic efficiency of Na plating and stripping on different electrodes. (e) Cycling behavior of symmetrical cells using Na and Na/NSCNT electrodes at 1 mA mA cm^{-2} and 1 mAh cm^{-2}, respectively. (f) The morphology change of Na/NSCNT electrodes before and after 20 cycles. Reproduced with permission.[42] Copyright 2018, Wiley-VCH. (g) Schematic of Na stripping and plating process on Na@CP-NCNTs. (h) SEM images of Na@CP-NCNTs after different stripping amount of Na in the first cycle. (i) Comparison of the cycling stability of the Na@CP-NCNTs and the bare Na foil at a current density of 5 mA mA cm^{-2} and 3 mAh cm^{-2}. Reproduced with permission.[43] Copyright 2018, Wiley-VCH.

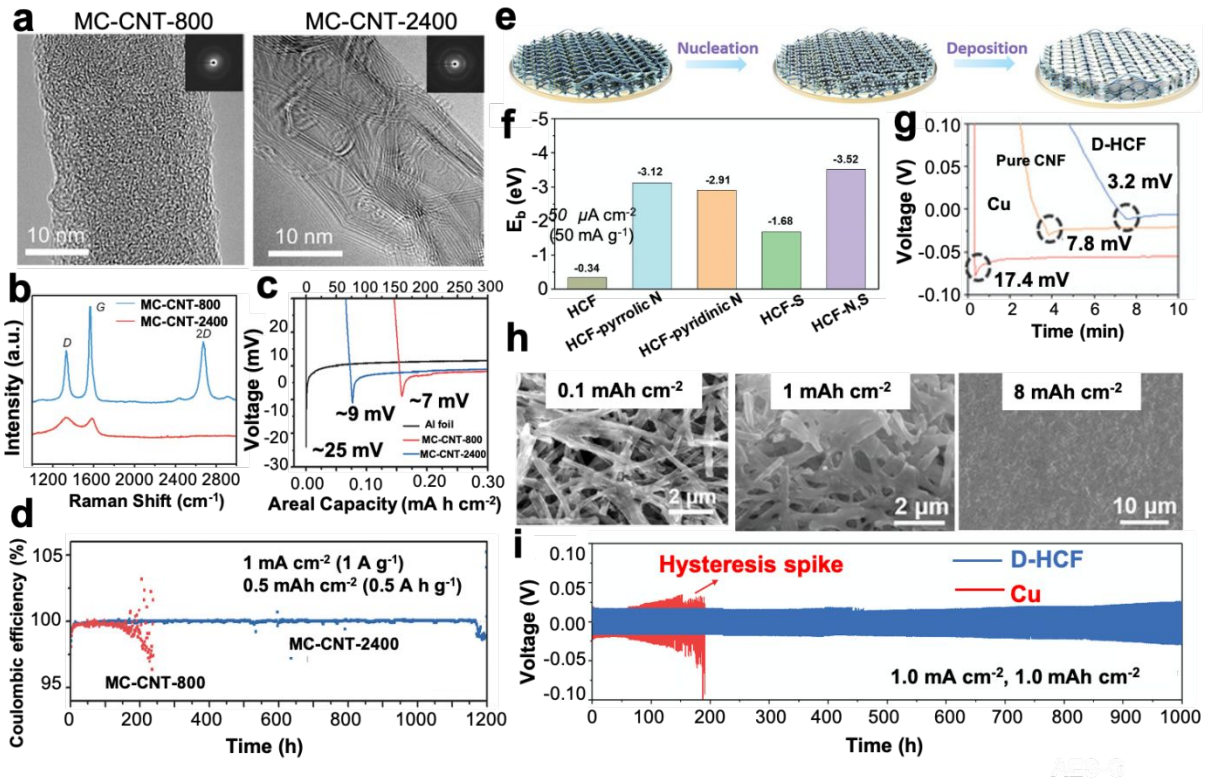

Figure 11. (a) High-resolution TEM images and (b) Raman spectra of MC-CNT-800 and MC-CNT-2400. (c) Galvanostatic discharge plots of MC-CNT-800, MC-CNT-2400 and Al foil at 50 μA cm^{-2}. (d) Cycling performances of MC-CNT-800- and MC-CNT-2400-based anodes at 1 mA cm^{-2} and 0.5 mAh cm^{-2}. Reproduced with permission.[44] Copyright 2018, Wiley-VCH. (e) Schematic of Na deposition process on D-HCF network. (f) Calculated adsorption energies of Na on various kinds of substrates. (g) Voltage profiles of Na deposition on planar Cu, pure CNF, and D-HCF electrode at 0.2 mA cm^{-2}. (h) Morphology evolution with different plated Na capacities on D-HCF network. (i) Galvanostatic volatage profiles of the symmetric cells using Na@D-HCF and Na@Cu electrodes at 1 mA cm^{-2} and 1 mAh cm^{-2}, respectively. Reproduced with permission.[45] Copyright 2019, Wiley-VCH.

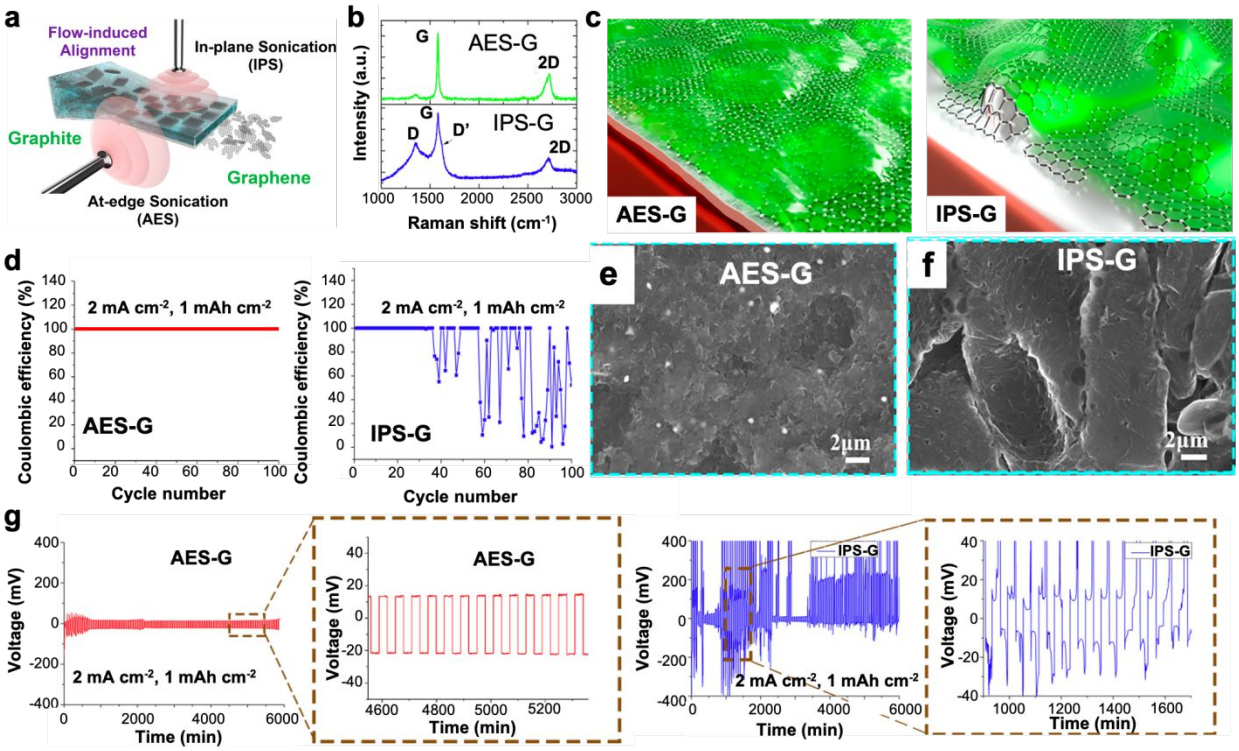

Figure 12. (a) Schematic illustration of the flow-aided sonochemistry exfoliation to achieve AES-G and IPS-G samples via tuning the orientation of the shockwave relative to the flow-aligned graphene flakes. (b) Raman spectra AES-G and IPS-G samples. (c) Schematic of SEI formation process on AES-G and IPS-G surface, respectively. (d) Coulombic efficiencies of Na plating and stripping on AES-G and IPS-G electrodes at 2 mA cm^{-2} and 1 mAh cm^{-2}. (e-f) SEM images of Na morphology deposited on AES-G and IPS-G substrates after 100 cycles. (g) Voltage profiles of Na plating and stripping for AES-G and IPS-G at 2 mA cm^{-2} and 1 mAh cm^{-2}. Reproduced with permission.[46] Copyright 2018, American Chemical Society.

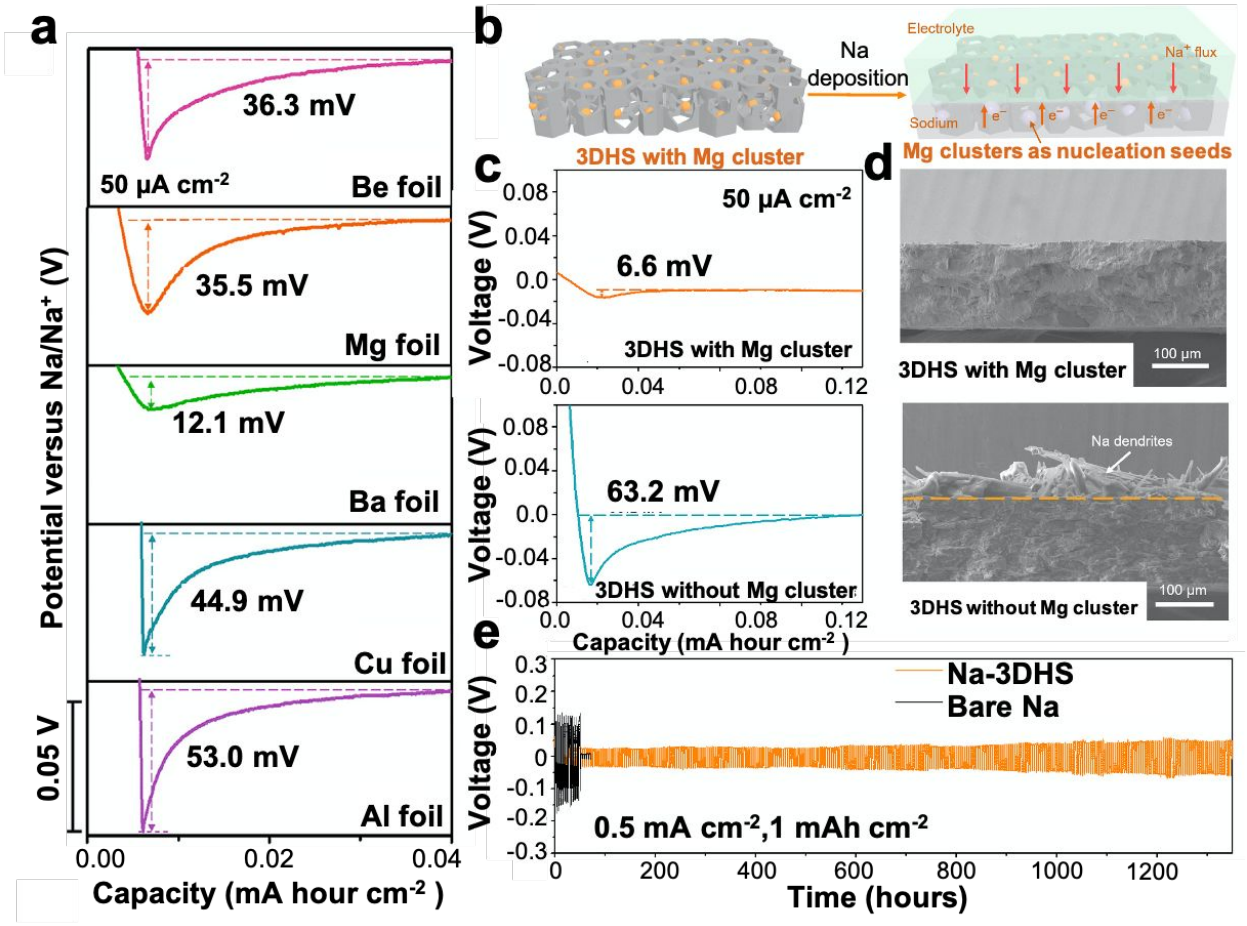

Figure 13. (a) Voltage profiles of Na deposition on different metal foils and respective nucleation overpotential at 50 μA cm^{-2}. (b) Schematic of Na deposition on 3DHS with Mg clusters. (c) Voltage profiles of Na deposition on 3DHS with or without Mg clusters at 50 μA cm^{-2}. (d) Side-view SEM images for deposited Na on 3DHS with or without Mg clusters. (e) Galvanostatic cycling stability of symmetric cells with Na-3DHS and bare Na electrodes at 0.5 mA cm^{-2} and 1 mAh cm^{-2}, respectively. Reproduced with permission.[47] Copyright 2019, American Association for the Advancement of Science.

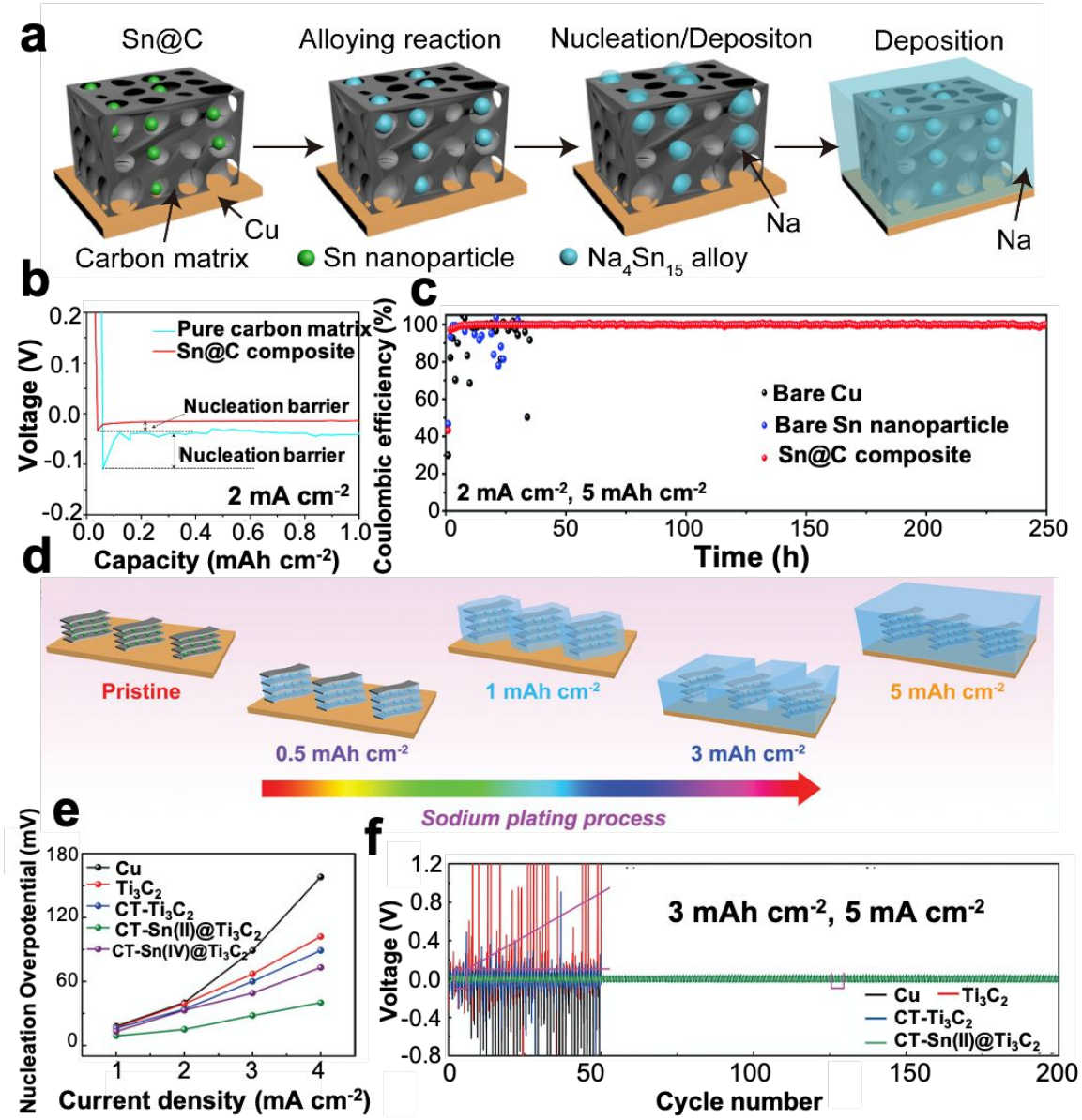

Figure 14. (a) Schematic illustration showing Na nucleation and growth on Sn@C composite substrate. (b) Voltage profiles on carbon network with or without Sn nanoparticles at 2 mA cm^{-2}. (c) Coulombic efficiencies on different substrates at 2 mA cm^{-2} and 5 mAh cm^{-2}. Reproduced with permission.[48] Copyright 2019, Royal Society of Chemistry. (d) Schematic diagram for Na nucleation, deposition in CT-Sn (II)@Ti_3C_2 matrix. (e) Summary of Na nucleation overpotential on different substrate at various current densities. (f) Galvanostatic cycling behaviors of symmetric cells made from different kinds of electrodes at 5 mA cm^{-2} and 3 mAh cm^{-2}. Reproduced with permission.[49] Copyright 2018, Wiley-VCH.

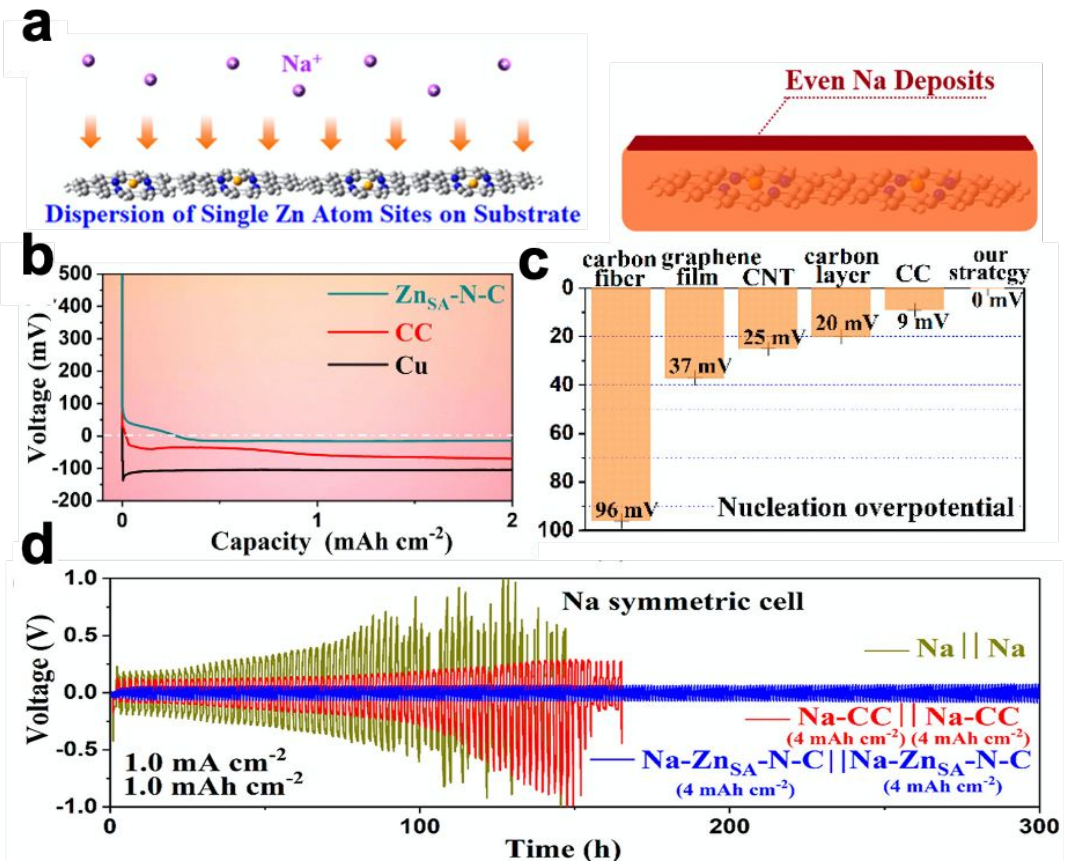

Figure 15. (a) Schematic illustration of Na plating behavior on Zn_{SA}-N-C substrate. (b) Voltage profiles of galvanostatic Na deposition on different substrates. (c) Nucleation overpotentials of Na deposition on different substrates. (d) Galvanostatic cycling stabilities of different electrodes in symmetric cells at 1 mA cm^{-2} and 1 mAh cm^{-2}. Reproduced with permission.[50] Copyright 2019, American Chemical Society.

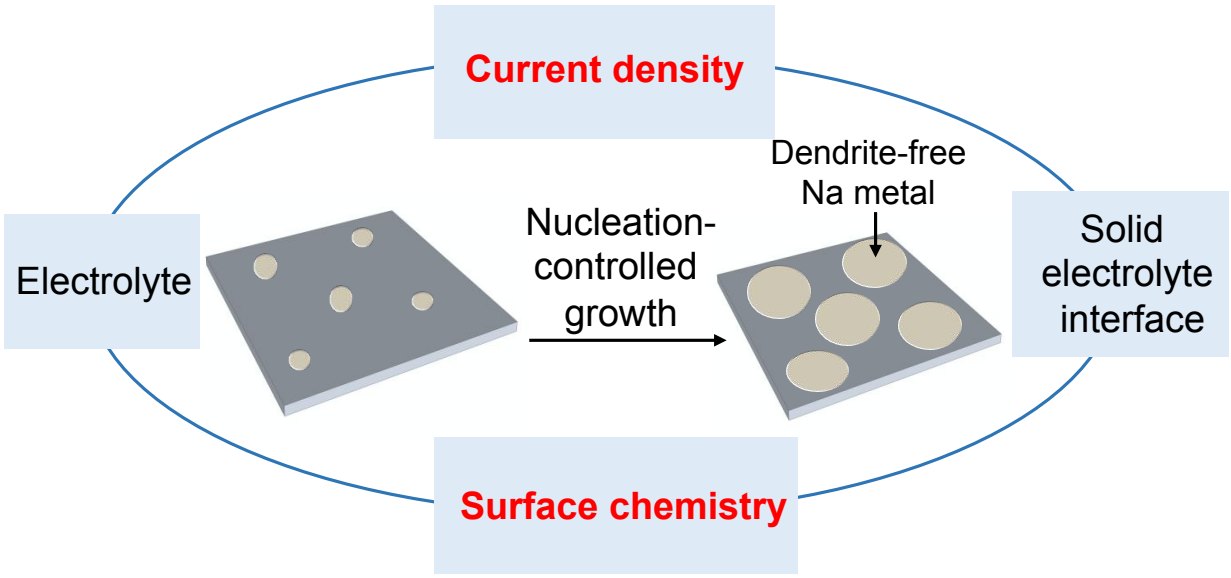

This review assesses both theoretical and experimental knowledge on sodium nucleation for the first time towards a safe sodium battery.